NEUTRON STUDIES OF UNDERDOPED SINGLE CRYSTAL $La_{2-x}Ba_xCuO_4$

NEUTRON STUDIES OF UNDERDOPED SINGLE CRYSTAL $La_{2-x}Ba_xCuO_4$

By

Jerod Justin Wagman, B.Sc.

A Thesis

Submitted to the School of Graduate Studies

in Partial Fulfilment of the Requirements

for the Degree

Master of Science

McMaster University

MASTER OF SCIENCE (2010)
(Physics and Astronomy)

McMaster University
Hamilton, Ontario

TITLE: NEUTRON STUDIES OF UNDERDOPED SINGLE CRYSTAL $La_{2-x}Ba_xCuO_4$

AUTHOR: Jerod Wagman, B.Sc (University of Toronto)

SUPERVISOR: Professor B, Gaulin

NUMBER OF PAGES: xvii, 98

Abstract

A series of elastic x-ray and inelastic neutron experiments have been conducted on $La_{2-x}Ba_xCuO_4$ (LBCO) crystals for $0 \leq x \leq 0.35$. We find that the dynamic correlations in the system are gapless and persist to at least order Kelvin temperatures. These features display qualitative and quantitative similarity to its sister compound $La_{2-x}Sr_xCuO_4$ (LSCO) for the same doping. We also find evidence that suggests connection between the dynamic rods of scattering and the pseudogap phase found in these materials, though nothing conclusive can be said at present. We will explore the doping, temperature and energy dependence of these dynamic features in detail.

Acknowledgements

I would first like to thank McMaster University and NSERC for their generous funding. Without them, this research would not been possible.

Next, I would like to thank my committee members, Bruce Gaulin, Graeme Luke and Maikel Rheinstadter for reviewing and hearing me defend this thesis. It is a great distinction to have such a distinguished committee and for this I am very grateful.

I would next like to thank my supervisor, Bruce Gaulin. His excellent wisdom and guidance were integral to the completion of this thesis. I am truly looking forward to continuing into my PhD under his supervision.

I must also acknowledge my wonderful group mates, Greg van Gastel, Patrick Clancy, Kate Ross, Jeremy Carlo, Katarina Fritsch and Jacob Ruff. In particular, I would like to thank Greg, Pat and Kate for tirelessly assisting me in this work. Kate not only contributed to the work at DCS, but also continually had great suggestions on how to use various computer programs, and is the creator of the wonderful phase diagram I use in the 7th chapter. Pat truly was a mentor to me during this work. He always had the best advice to offer, be it on data analysis or on how to handle situations in general. I give very special thanks to my partner in this work: Greg. It was an honour and distinction to work with him, and I will miss discussing the physics of LBCO with him, and watching youtube videos in the Sequoia hutch with him as I continue forward.

I would also like to thank all my wonderful friends for their support in this time. In particular, I would like to acknowledge Bram Smagalla, Nick Concepcion, Sarah McNeil, Sarah Purdy, Nathan Leigh, Mark Healy, Matt Minnick, Travis Williams, Adam Aczel, Vega Janic, Tara Parkin, Robbie Henderson, Andrew Obradovich, Leo

van Nierop, and Fiore Carpino. These people were tremendous sources of strength and support throughout my thesis. Extra special thanks goes to Ben Jackel. From teaching me gumdo, dungeons and dragons and talking to me at least weekly about my research, his time was invaluable to this project.

I of course also want to thank my family: Charles Wagman, Francine Sherkin, Annie Murray, Ruth Sherkin and Joe Sherkin. They all put up with me for years and have been a constant source of strength for me. My dad must receive special credit though for being the poor soul who proof read this monstrously long work. As he does not understand physics, this task was made all the more difficult.

Lastly, I want to thank my wonderful girlfriend Dana Doidge. The last few months of my thesis were by far the toughest and she was a rock for me to cling to to weather the storm. I of course also need to thank her for allowing me to speak incomprehensible physics at her. It warmed my heart that she would listen patiently to me.

Thank you with all my heart to all those listed here and those I did not have space to list. I can be as strong as I am only because of the wonderful family, friends, and colleagues I have had the great fortune to work with.

Dedicated to....Boobie and the memory of Zaidy. I could not have done all I have without you.

Table of Contents

List of Figures

List of Tables

Chapter 1

Introduction

Josephson junctions, stable, resistanceless currents for MRI's, levitating trains, lossless energy transmission. These wonders and more are all advents due to the superconducting state. Furthermore, superconductivity is a macroscopic quantum mechanical state. It is obvious from this that the study of superconductivity is of interest both industrially, i.e. from a technological perspective, and theoretically, i.e. from a desire to have a fundamental understanding of the universe in which we exist.

In 1986 [13], high temeperature superconducting materials were discovered. It is unclear why these materials possess elevated superconducting transition temperatures. Transitions to the conventional superconducting state ground state, as well as low lying excitations therein, were explained in 1957 [14]. To date, no analog of this understanding exists for high temperature superconductors. Given the intellectual drivers for understanding of superconductivity in general, it is clear that the lack of detailed knowledge about the high temperature superconducting state is unacceptable.

That said, progress has been made in this problem. Furthermore, it has been put forward that the superconductivity seen in organic superconductors and heavy fermionic superconductors [15] may be of the same origin as high temperature superconductivity. Though satisfactory intuition in these systems is lacking considerable understanding exists.

Recently, the pnictide high temperature superconductors were discovered. These materials contain many hall marks seen in cuprate based high temperature superconductors [16]. As in the cuprates, an antiferromagnetically ordered state gives way to superconductivity upon appropriate substitution of atoms in the crystal lattice. Confusingly, in the pnictides it does not appear that there is a direct link between the introduction of holes to the superconducting plane and superconductivity. It is believed that is the introduction of holes that drives both superconductivity and magnetism in the cuprates [3].

Regardless, it is clear that there are ties between magnetism and superconductivity [3]. What is not clear is in what way these two features interact. Does one give rise to the other or is the relationship more symbiotic? Experimentalists have been hard at work for over 20 years trying to ellucidate this relationship.

Critical to this search is neutron scattering. We are dealing with long range order and magnetism. Neutrons lend themselves naturally to this study as they are arguably the most important probe of long range magnetism, as will be explored in this thesis. The prominent role neutrons will play implies the need for large pristine single crystals. For $La_{2-x}Ba_xCuO_4$ (LBCO), this

has only been possible in the last few years. It is due to this recent advance in crystal growth that the present studies in LBCO became practical.

The goal here is to study the low doping regions of the LBCO phase diagram, i.e. $x \leq 0.035$. This doping regime is not superconducting and the crystal structure is purely orthorhombic for the temperatures that will be considered. Despite neglecting the superconducting aspect of these materials in this study, a rich and diverse magnetic system still remains. Furthermore, there are only magnetic transitions to consider here. Thus, our description of the system can be relatively simple.

What we will consider here is a range of single crystal LBCO of doping $0 \leq x \leq 0.035$. These crystals have been examined with neutron instruments at Chalk River National Laboratories, Oak Ridge National Laboratories and the National Institute of Standards and Technology, as well as with x-rays at McMaster University. What we will find is that this system is identical qualitatively to many other cuprate superconductors. We will also find that in instances where numerical comparison is possible that LBCO is identical to many other cuprate superconductors quantitatively as well. The importance of this result is that it is a result that is consistent with the hypothesis that it is the introduction of holes into the system that drives the magnetism seen in these cuprate systems.

Chapter 2

The LBCO System

2.1 Introduction

In this chapter, we will discuss background information about the LBCO system. We will also discuss the sister compound LSCO ($La_{2-x}Sr_xCuO_4$). A main focus of this thesis will be to show that LSCO and LBCO have the same magnetic correlations. Hence, it is imperative to explore some key observations for the LSCO system. The structure of this chapter is is as follows. We will discuss the chemical structure of the La based cuprates and conclude with a survey of the observed magnetic structure in LSCO.

2.2 Chemistry

The parent compound La_2CuO_4 is a layered structure. At temperatures well over 400 K [17], it is tetragonal with space group I4/mmm. The tetragonal unit cell has a and b axes which are parallel with nearest neigbour copper atoms in the copper-oxide plane. At ambient temperatures and below, it is an orthorhombic structure with spacegroup Bmab and lattice parameters a =

5.343, b = 5.401 and c = 13.153 in $\mathring{A}$ [11]. The orthorhombic unit cell as a and b axes which run between next nearest neighbour copper atoms in the copper-oxide plane. All temperatures considered in this thesis are ambient or lower. We will use the tetragonal notation predominantly as this is a simpler unit cell with which to understand the physics. Assuming that we have a tetragonal unit cells we arrive at approximate a and b lattice parameters of 3.78 $\mathring{A}$. The chemical structure of the parent compound is shown in figure 2.1.

The driver of the physics in this system is the substitution of an atom with a charge of 2+ for the ^{3+}La in the lattice. The superconductivity and magnetism in this system resides in the copper-oxide plane. Hence, the function of doping is to substitute holes into the copper-oxide plane. Thus, accurate quantification of the doping process is essential. Concern is also placed on oxygen concentration for this same reason. However, as seen in figure 2.2, measurement of the orthorhombic transition temperature offers a measure of the doping level in a system. Quantification of the amount of oxygen in the system has not been successul to date in our LBCO crystals. However, by growing all crystals under the same conditions, we do maintain a consistent quantity of oxygen in the lattice. Previous measurements suggest that the oxygen content is greater than 4 per formula unit. Therefore, all our measured values should be consider as though we were at slightly higher dopings than are reported. This is a small perturbation that should be kept in mind going forward.

Let us turn our attention to comparison of the crystal structures of LBCO and LSCO. Note, that Ba is a larger atom than both Sr and La. Therefore, we

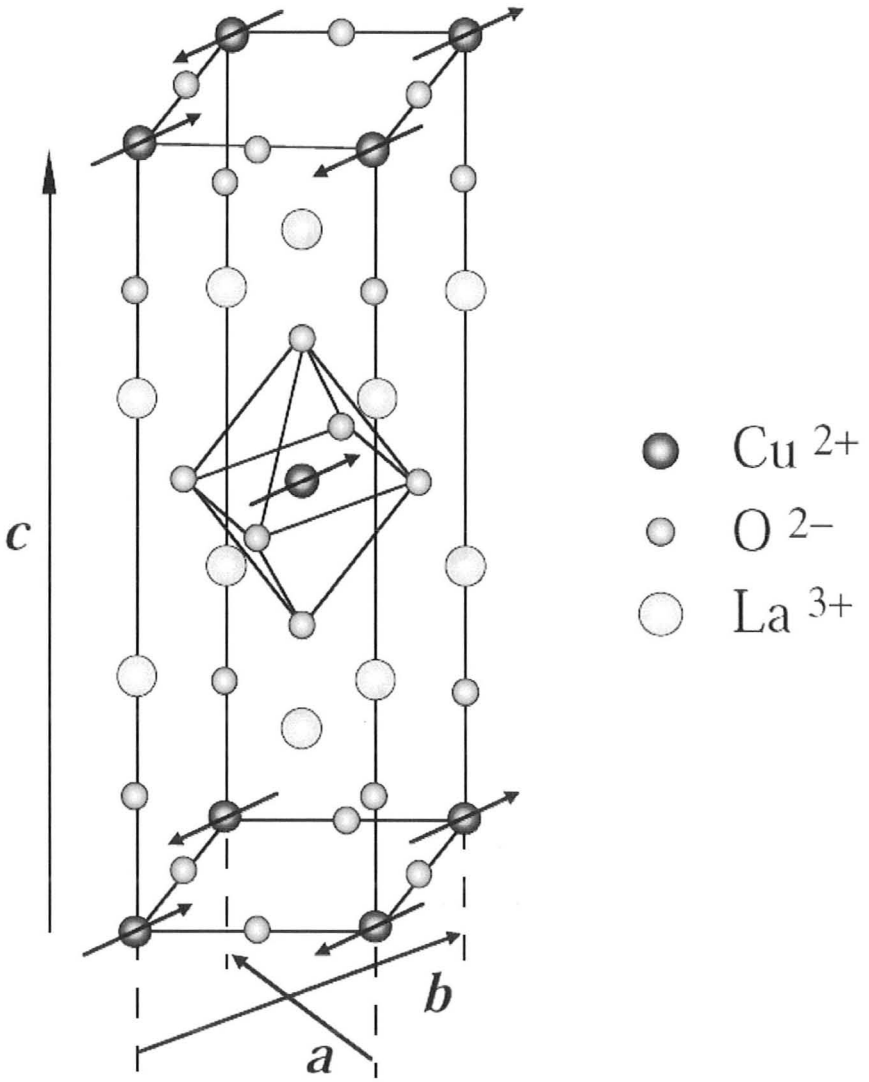

Figure 2.1: Chemical structure of La_2CuO_4 [1]

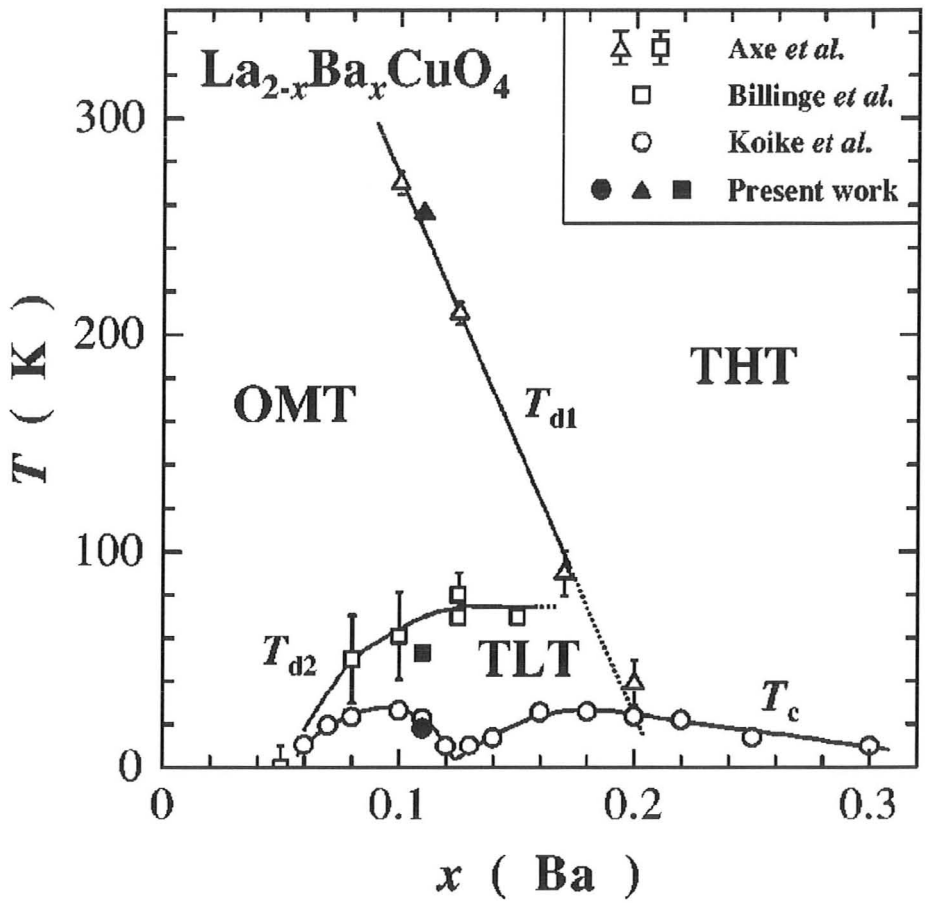

Figure 2.2: Structural phase diagram for LBCO [2]

may expect some crystalographic differences due to the introduction of such a large atom. Despite this, at the dopings we will consider the effects of this substituion on the crystal lattice is negligible at the temperatures we will consider. Though the transition between the high temperature tegragonal (HTT) phase and the medium temperature orthorhombic (MTO) phase does decrease with doping, the transition temperature remains well above all temperatures we observe. This is summarized succinctly in figure 2.2. The HTT→ MTO transition is second order.

2.3 The Magnetic Structure of LSCO

The phase diagram for LSCO is shown in figure 2.3. At the lowest dopings, the material is a Mott insulating, three dimensionally ordered antiferromagnet. Simultaneous with this three dimensional antiferromagnetic ordering, there is a a static spin glass state. Since the publication of the phase diagram shown here, it has been shown that this spin glass state is a two dimensionally ordered, incommensurate, antiferromagnet [3]. For $x \geq 0.02$, the three dimensional ordering is extinguished. However, the spin glass state persists throughout the remainder of the phase diagram. The incommensurability of this state increases with doping in this doping region. For $x \leq 0.5$, this two dimensional rdering is diagonal with respect to the tetragonal unit cell. In the superconducting dome, the ordering is parallel to the tetragonal unit cell.

What is not shown in this phase diagram is the spin dynamics of the system. It has been observed that dynamic two dimensional magnetic correlations appear at the same wavevector as the static magnetic order. The incommensuration of this correlation decreases on increases in temperature. Like the two dimensional static magnetic ordering, this dynamic correlation's incommensurability scales with doping in the same way as the static two dimensional magnetic ordering [3].

These dynamic spin correlations also show dispersion [4]. This phenomenon takes the shape of an hour-glass and is shown in figure 2.3. As energy transfer increases, incommensuration decreases until a minimum is reached. The point at with the highest density of states is referred to as the resonance. This feature also has a doping dependence, which is shown in figure 2.3.

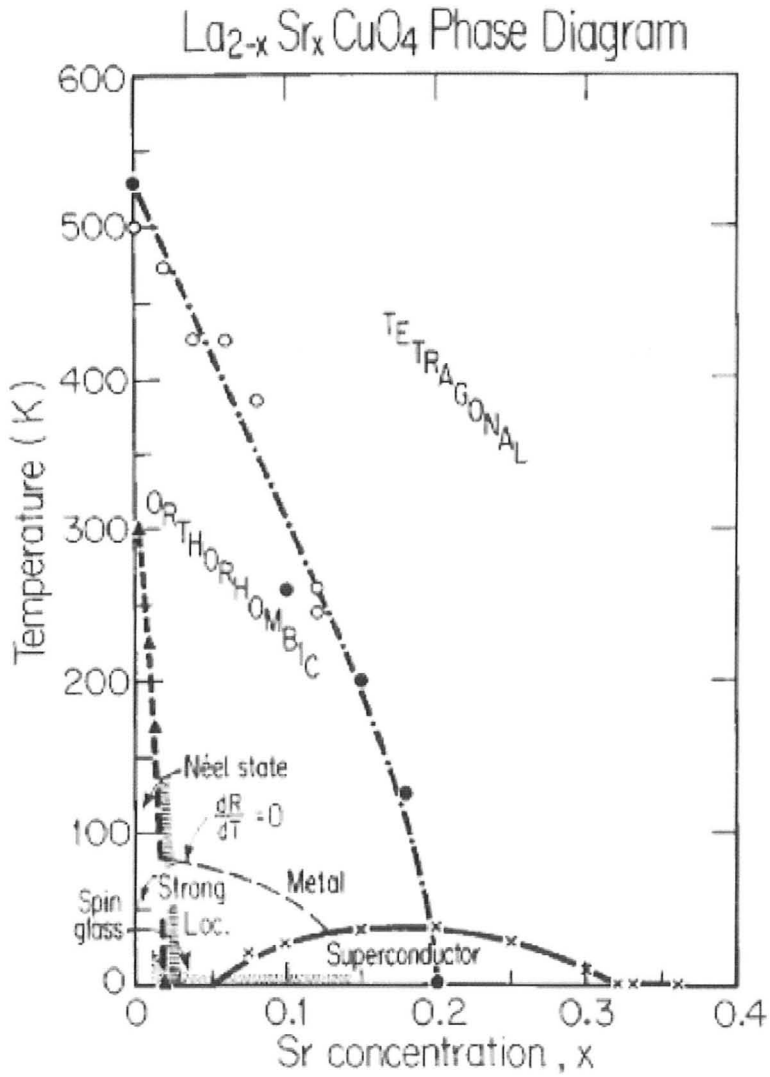

Figure 2.3: LSCO phase diagram [3]

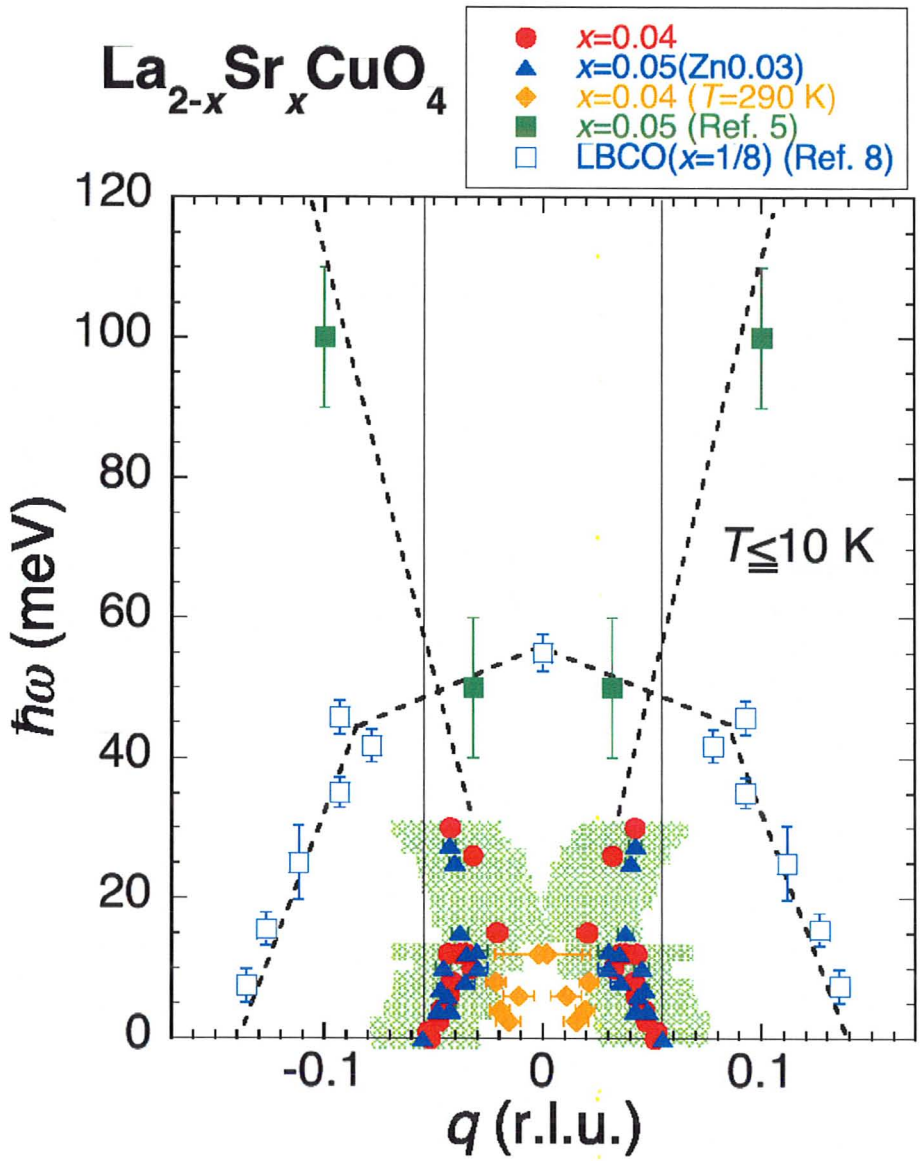

Figure 2.4: Dispersion of the dynamic magnetism in LBCO. This data is based on a series of observations. Notice the overall dispersion shape is that of an hour glass for the x = 0.04 data. This is the most important data to consider here as it is this data we seek to correlate with our data for LBCO [4].

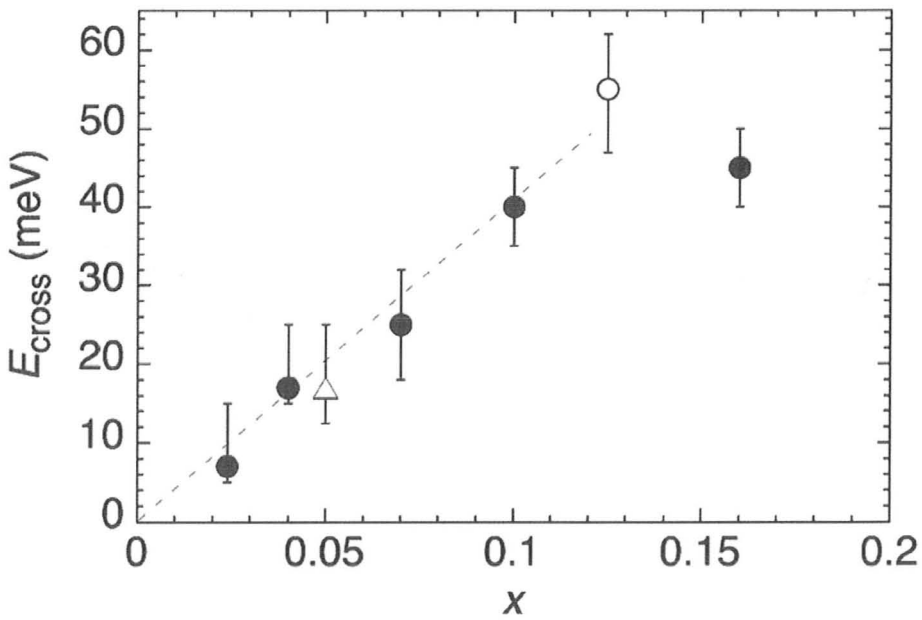

Figure 2.5: Doping dependence of the resonance energy. Notice for x = 0.04 that the energy is around 8 meV. The difficulty in pinning down the error bar above this energy is due to the presence of phonons. This is a key point as it is this data we will compare to LBCO [4].

There are two competing pictures to explain these dynamic spin correlations: the stripe and itinerant pictures [18, 19]. They are mentioned as these models have been employed to explain the existence of the magnetism we will discuss in this thesis. The results presented here do not impact this discussion in any definitive way. Hence, the details of these pictures will not be discussed here.

Chapter 3

The X-Ray Diffraction Technique

3.1 Introduction

In this thesis, the only diffraction, i.e. elastic scattering, experiments we will discuss are those that involve x-rays. This is a special case of the general formalism of scattering that will be considered in chapter 4. However, to fully appreciate what can be done in an x-ray experiment, we must consider the details of elastic scattering. In this vein, we will first discuss the basics of diffraction. We will then consider some x-ray specific nuances of diffraction, which will include the production of x-rays and the experimental setup employed in the x-ray diffraction experiment examined in this thesis.

3.2 Diffraction

3.2.1 Basics

Quantum mechanics stipulates that particles also have a wave based nature. Therefore, if one were to scatter particles of wavelength λ, off of a crystal lattice, with a lattice spacing in some direction of d, one would expect to see diffraction provided $\lambda \leq d$. Now, typical atomic separations in crystals are on the order of $\mathring{A}$. For x-rays, E = pc = $\hbar\omega$. Numerically, this works out to the x-rays having an energy on the order of keV.

To develop the formalism of diffraction in crystals, let consider the von Laue formulation of diffraction [5]. For the time being, we will assume that there are two identical atoms separated by a distance R. Suppose radiation of wavevector **k** scatters elastically from the two atoms to a new wavevector **k'**. Let $\hat{\mathbf{n}}$ and $\hat{\mathbf{n}}$' be parallel to **k** and **k'** respectively. This arrangement is shown in figure 3.2.1. As we will be extending this logic to a crystal lattice, note that a vector of length R connecting the two atoms will simply be a lattice vector.

We can rewrite any wavevector as

$$\mathbf{k} = 2\pi\hat{\mathbf{n}}/\lambda \tag{3.1}$$

Since we assume elastic scattering, both wavevectors in this problem have the same wavelength, but differing propogation directions. From the geometry in figure 3.2.1, we can see that we will have constructive interference if

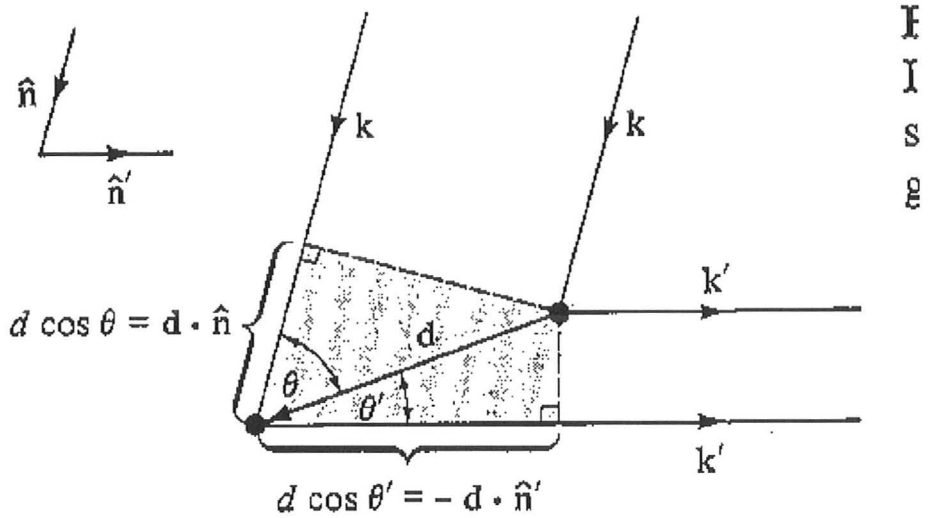

Figure 3.1: Diagram of geometry in the Laue formulation of diffraction [5]

$$Rcos(\theta) + Rcos(\phi) = \mathbf{R} \bullet (\hat{\mathrm{n}} \text{ - } \hat{\mathrm{n}}') \tag{3.2}$$

For constructive interference, the path difference must be an integer, m, times λ. So this is

$$m\lambda = \mathbf{R} \bullet (\hat{\mathrm{n}} \text{ - } \hat{\mathrm{n}}') \tag{3.3}$$

By dividing through by $2i\pi/\lambda$ and raising both sides of the equation as powers of e yields

$$e^{i(\mathbf{k} \text{ - } \mathbf{k}') \bullet \mathbf{R}} = 1 \tag{3.4}$$

This is the condition for a reciprocal lattice vector. Therefore, there will be constructive interference only if the difference in radiation vectors, called the scattering wavevector, is a reciprocal lattice vector. Given this condition, we can therefore extend this formalism to any pair of scatterers and can therefore generalize these results to be applicable to an entire crystaline lattice.

Let us now turn to the Ewald Construction, shown in figure 3.2.1 [5]. Suppose we kept the incident wavevector fixed but rotated the crystal. This will map out a circle in reciprocal space. Let us place the tail of the incident wavevector on a reciprocal lattice point. Since the scattering wavevector has the same length as the incident wavevector, only reciprocal lattice points that lie on the radius of the circle can define a reciprocal lattice vector such that $\mathbf{k} - \mathbf{k}' = \mathbf{K}$. This concept is easily generalized to three dimensions as a sphere, known as the Ewald sphere. The surface Ewald sphere spans all reciprocal lattice points, and by extension all reciprocal lattice vectors, that one can probe by diffraction for the given incident wavevector.

To conclude our survey of diffraction let us develop the Bragg formulation of diffraction. With some simple geometry, we can construct this formulation from the Laue formulation. The geometry of this is shown in figure 3.2.1. We first note that for any family of lattice planes separated by a distance R, there are reciprocal lattice vectors perpendicular to the plane. Of these vectors, the shortest vector has a length of $2\pi/d$ [5]. Further note that all perpendicular reciprocal lattice vectors are just integer multiples times longer than this shortest reciprocal lattice vector. This guarantees that

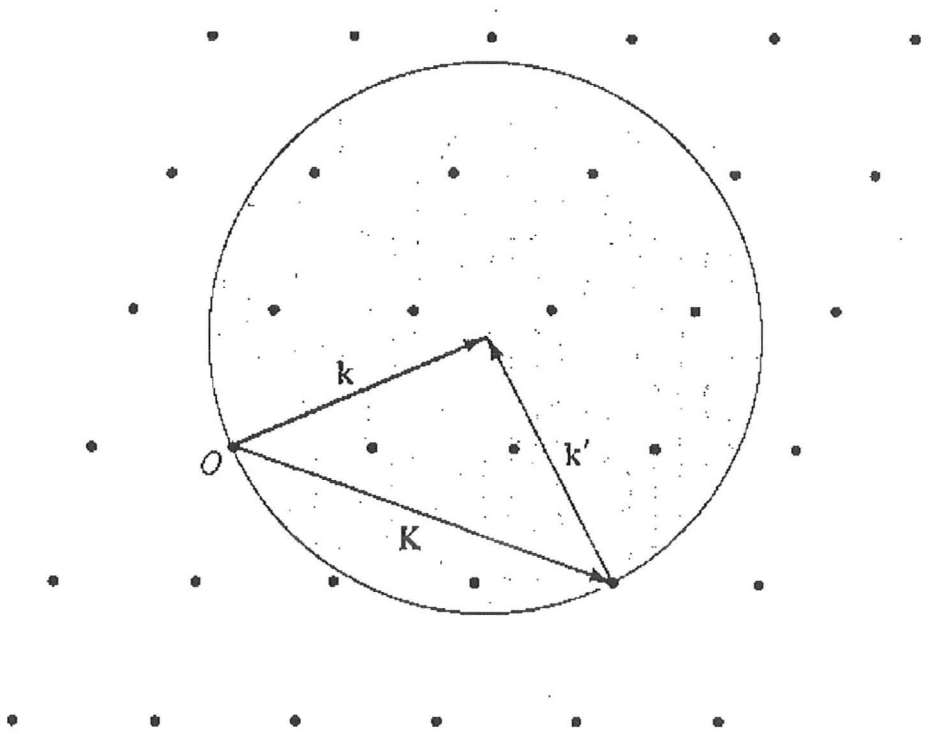

Figure 3.2: The Ewald Sphere [5]

$$K = \frac{2\pi n}{d} \tag{3.5}$$

for integer n. Now consider figure 3.2.1. We see that

$$K = 2ksin(\theta) \tag{3.6}$$

This implies that

$$ksin(\theta) = \frac{n\pi}{d} \tag{3.7}$$

Given the relation between wave number k and wavelength λ we have

$$n\lambda = 2dsin(\theta) \tag{3.8}$$

Equation 3.8 is Bragg's law. Bragg's law specifies where to expect radiation incident to a lattice plane at angle θ to scatter to. This is what allows the construction of all the neutron and x-ray diffracometers we use today.

3.2.2 Structure Factors

So far, it was assumed that the scattering entities were identical atoms that are part of some simple lattice structure. This negelcts that in general, we will be concerned with an array of different atoms in a given lattice that may require a lattice with a basis to describe. We must therefore extend our formalism further.

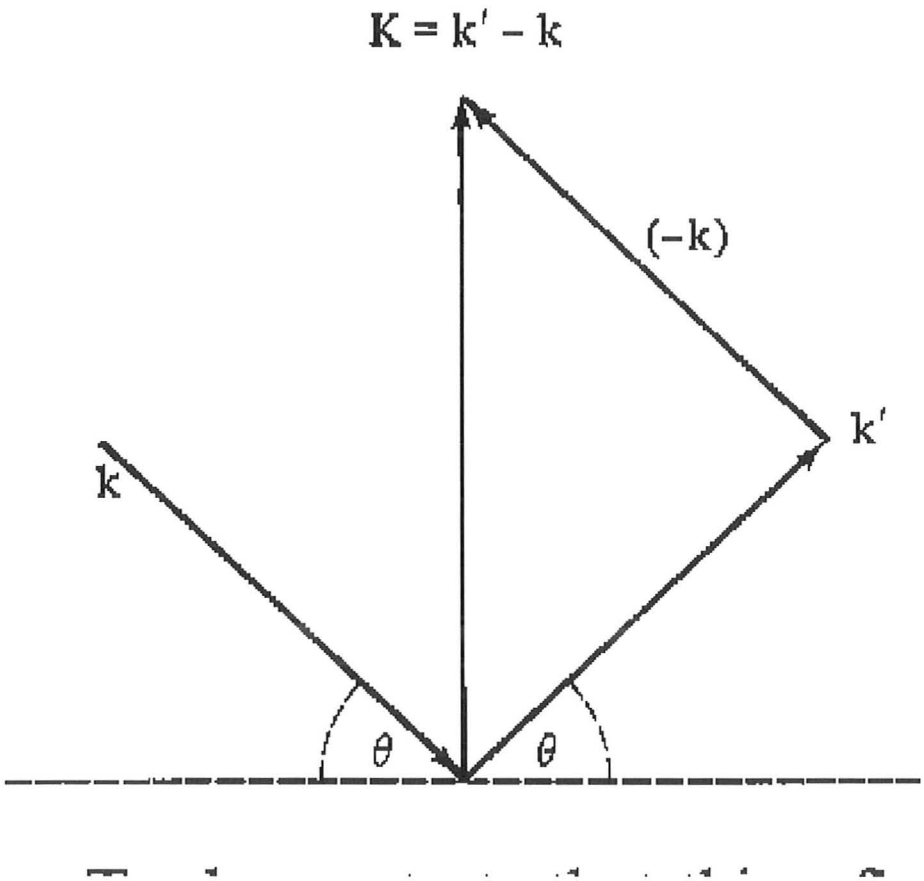

Figure 3.3: Geometry to map between the Laue and Bragg formulations of diffraction [5]

The first extension encapsulates generalized structure. Suppose a lattice of interest could be described as a lattice with a basis. Namely, let $\mathbf{R}_1$ to $\mathbf{R}_n$ span the crystal lattice. As discussed above, this yields a set of Laue conditions. We can encode all of these at once by defining

$$S_{\mathbf{K}} = \sum_{j=1}^{n} e^{i\mathbf{K}\bullet\mathbf{d}_j} \tag{3.9}$$

which is the geometrical structure factor. This allows us to mathematically encode interference effects from scatterers at different positions. However, as defined, we still assume all scatterers are identical.

To develop the geometrical structure factor into a general form factor that describes different scatterers at different locations is natural from here. For simplicity, we will restrict ourselves to the case of x-rays. For x-rays, the mediating interaction is electromagnetic. As the magnetic interaction for x-rays is weak, we can neglect this and instead posit the intereaction is entirely electric. Therefore it is the charge density that is key. Elementary treatments show that [5]:

$$f_j = -\frac{1}{e}\int d\mathbf{r} e^{i\mathbf{K}\bullet\mathbf{r}}\rho_j(\mathbf{r}) \tag{3.10}$$

The quantity f_j is known as the atomic form factor. Combining this result with the concept of the geometric form factor allows for the definition of an overall form factor for x-rays called the scattering function $S_{\mathbf{K}}$. Mathematically,

$$S_{\mathbf{K}} = \sum_{j=1}^{n} -\frac{1}{e} \int d\mathbf{r} e^{i\mathbf{K}\bullet\mathbf{r}} \rho_j(\mathbf{r}) e^{i\mathbf{K}\bullet\mathbf{d}_j} \tag{3.11}$$

The scattering function is related to the net intensity through its magnitude squared. There are other proportionality factors in the intensity itself, but the physics is encoded in the scattering function.

3.2.3 X-Ray Properties and Production

Recall we deduced that our x-rays will have order keV incident energies. At order keV energies, the mean free path of x-rays is approximately $5\mu m$ [20]. This is small relative to typical sample thickness. Therefore, in order to measure any intensity, one will usually require the detector to be in a setup to measure reflected x-rays as transmitted intensities will be negligible.

The basis of x-ray production is the acceleration of charges. From electromagnetic theory, an accelerating charge will emit radiation with a frequency that depends on the magnitude of the acceleration. The apparatus we will use for x-ray production of radiation is the rotating annode. The physics of the rotating anode, at the qualitative level, is straight forward. Electrons are accelerated by a potential gradient. This leads the electrons to follow a path that is intersected by a target material (the rotating anode). A collision ensues, decelerating the electrons. This will therefore in turn emit radiation. The maximum possible deceleration has an upper limit set by the voltage being applied [6]

$$eV = \hbar\omega_{max}$$

$$\lambda_{min} = \frac{2\pi c}{\omega_{max}}$$

$$=> \lambda_{min} = \frac{2\pi\hbar c}{eV} \tag{3.12}$$

As there are many electrons, we expect an equilibriation of the electrons and hence we predict a continuous spectrum of x-ray frequencies produced by this method.

There is a second advantage to using a target as the decelerating medium. If the energy transfered to the target material is sufficiently high, electronic state transitions can also occur. This kind of absorbtion can be thought of as a resonance. If one were to plot measured intensity vs. wavelength, there would be a spike in intensity everytime an electronic transition would occur. This is shown in figure 3.2.3.

The net intensity will scale with the power used to accelerate all the incident electrons. It is therefore advantageous to maximize the power of the accerating potential. Clearly, this will yield multiple electronic transition peaks at well defined wavelengths. In the x-ray experiments we will consider, as purely a monochromatic beam as possible is required to be incident on the sample. To resolve this issue, a monochromator is used. This utilizes Bragg's law. Recall that the transition peaks are of unique frequencies. Hence, by placing a properly oriented Bragg plane, oriented such that only Bragg reflected x-rays will travel towards the sample, then the beam that reaches the sample will be nearly monochromatic. Of course, integer multiples of the desired frequency

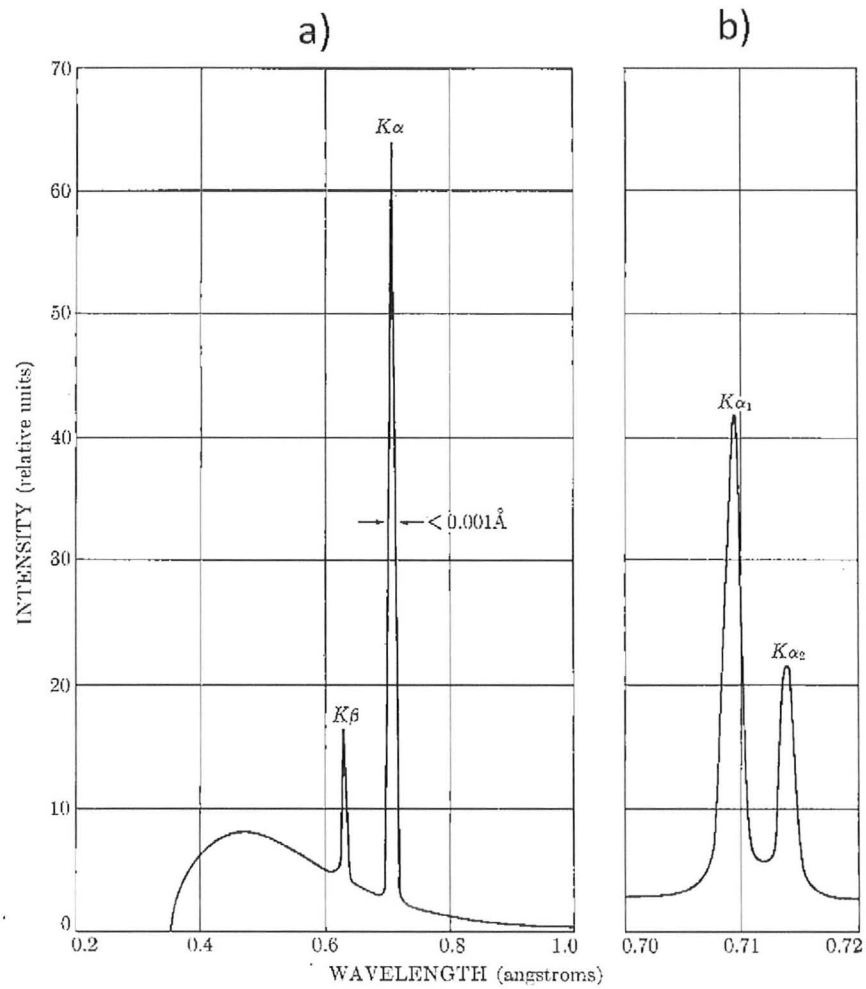

Figure 3.4: Spectrum of produced radiation for Mo using a 35 kV accelerating potential. a) This pannel displays two resonance features in intensity due to electronic transitions. b) Closer examination of the K_α peak displays there is fine structure. There are actually two electronic transitions at nearly the same wavelength.[6]

will travel to the crystal as well. This signal is typically weak and with proper electronic setup, this effect can reduced to acceptable levels for the purposes of experimentation.

Let us conclude this chapter by briefly stating some typical Cu k_α radiation wavelengths that are used in McMaster based rotating anode measurements [20].

$$\begin{aligned} K_{\alpha 1} &= 1.54051\mathring{A} \\ K_{\alpha 2} &= 1.54433\mathring{A} \\ K_{\beta 1} &= 1.39217\mathring{A} \end{aligned} \tag{3.13}$$

Chapter 4

Neutron Scattering

4.1 Introduction

Neutron scattering is a powerful probe of condensed matter. The mediating interactions for neutrons with matter are the strong and magnetic interactions. Also, the neutron-nucleus cross section depends on the nuclear structure as opposed to the charge density. Therefore, the neutron scattering cross section will have a different structure as a function of atomic number than x-rays.

The main limitation of the neutron is that in experimental practice, neutrons are produced at low fluxes and high costs. For research applications, neutrons are created at reactors and spallation sources. Even with cutting edge technology, fluxes of neutrons are still behind the x-ray production capabilities of an in-house x-ray source. This will affect the power of the statistics that can be gained during an experiment.

Despite this limitation, neutrons are an invaluable probe. We know that neutrons are capable of scattering. However, the neutron is a massive particle, whereas the x-ray is massless. The wavelength of a particle is determined by

its total energy. This implies that the kinetic energy of a neutron necessary for order angstrom wavelengths is order meV. Note, this kinetic energy is a million times smaller than the kinetic energy of a typical x-ray used in diffraction. As inelastic scattering will affect the kinetic energy scattering particle, and typical excitations in condensed matter are order meV, a typical neutron experiment is well suited to making observations about excitations in a condensed matter system.

In this chapter we will examine the theory of neutron scattering. Ths first section will closely follow Squires' [7] first two chapters, and will develop a general formalism for scattering off of some potential V. The next section will then formulate some of the basic theory of magnetic scattering. This section will follow the seventh chapter of Squire's text. This chapter will conclude with sections on the setup of a triple axis spectrometer and a time of flight spectrometer.

4.2 Basics of the Neutron

The charge of a neutron is zero for all condensed matter applications. Therefore, the neutron-matter cross section is rather low. As a result, the neutron mean free path is quite long and hence neutrons can sample the physics througout a given sample. Additionally, unlike for x-rays, charge neutrality implies that the neutron can explore bare hard core interactions.

A powerful aspect of using the neutron as a probe is that it is massive. The mass of the neutron is 939.573 MeV/c^2 [21]. Thus, to obtain order $\mathring{A}$ neutron wavelengths requires only order meV kinetic energies. Now, condensed matter

Table 4.1: Basic Neutron Properties [7]
mass = 1.675 x 10^{-27} kg
charge = 0
spin = $\frac{1}{2}$
magnetic moment = -1.04 x $10^{-3}\mu_B$
kinetic energy of standard thermal neutron at room temperature = 25.3 meV

excitations are largely on the order of meV. These points together imply that one can easily distinguish elastically scattered neutrons from those that are inelastically scattered.

Neutrons are also spin $\frac{1}{2}$ particles. This implies they have a magnetic moment and hence can couple magnetically. This interaction can be more subtle to detect with neutrons alone because neutrons also interact via the strong force. However, magnetic and structural signals can be distinguished in many ways. The method employed in our study of the LBCO crystal is that the combination of x-ray data with neutron data. Recall that we can probe the temperature dependence of the crystal structure with x-rays. By considering this information, it is then possible to distinguish magnetic and structural scattering. In this way, for example, neutrons offer an unambiguous and direct measure of the magnetism in a system.

Table 1.1 summarizes these above points.

A final note to make about the neutron is that its low kinetic energy translates tol velocities that are typically on the order of km/s. This implies that one can use Maxwell-Boltzmann statistics to analyze neutron velocity distributions for a given temperature. By having the neutrons thermalize in a moderator of a known temperature, one can therefore have most neutron velocities be of a

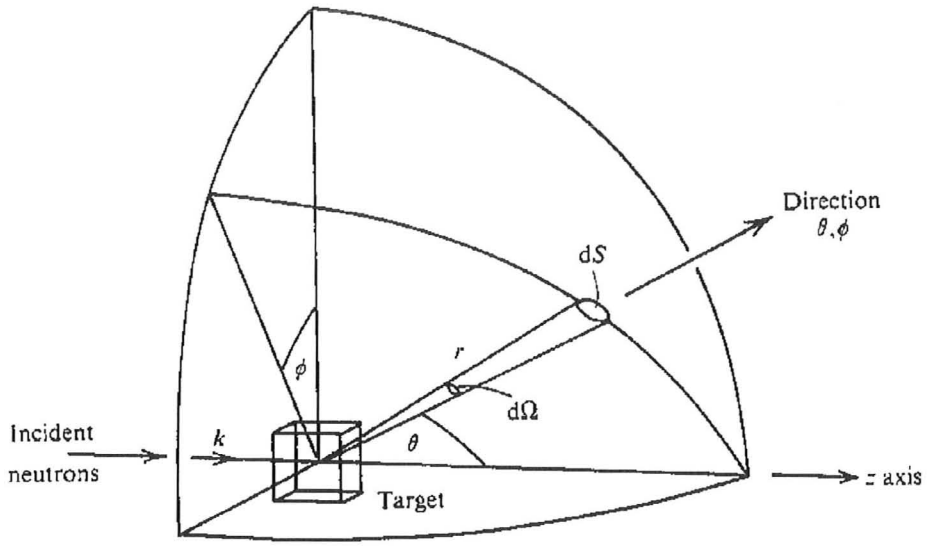

Figure 4.1: Geometry of a general scattering experiment. This figure defines all the quantities from which we can calculate the scattering cross section. [7]

certain desired value prior to any beam monochromation. Typical moderators are liquid hydrogen for slow ($\leq$10 meV) neutrons, heavy water for thermal neutrons ($\leq$100 meV) and graphite for fast neutrons (100-500 meV) [7].

4.3 Nuclear Scattering

Figure 4.1 shows the geometry of a scattering experiment. In practice, we deal with monochromatic beams. Therefore, let us assume we have a well collimated beam of wavevector **k** and energy E. Let us now suppose we set up our detector so that by either measuring the time of flight or by use of Bragg's law that we can measure outgoing neutrons of wavevector **k'** and energy E'. Assume the target to detector distance is large. This problem is simplest to treat mathematically in polar coordinates. We define the partial differential cross section as the number of neutrons scattered per second into $d\Omega$, with

energy between E' and dE' with wavevector **k'**. We normalize this by solid angle, energy range and incident flux. We also define the differential cross section as the number of neutrons scattered per second into solid angle $d\Omega$. Mathematically we write:

$$\frac{d\sigma}{d\Omega} = \int_0^\infty (\frac{d^2\sigma}{d\Omega dE'})dE' \tag{4.1}$$

We further define the total cross section by

$$\sigma_{tot} = \int_{alldirections} (\frac{d\sigma}{d\Omega})d\Omega \tag{4.2}$$

Let us approximate that we are dealing with a single fixed nucleus. Let us also use the Born approximation and assume our incident and outgoing neutrons are plane waves defined by their wavevectors. Take the origin to be the position of the nucleus. As we are concerned with solids, stationary nuclei is a sensible approximation. Our incident neutrons can be expressed as plane waves. Let us further assume that the nuclei is a point source and hence the scattered neutrons are scattered with spherical symmetry from the nuclei. The basis for this is that atomic nuclei are miniscule by comparison to size of atom, which is smaller than the interatomic distance, which is same scale as the wavelength of the neutron. As we are dealing with scattering, we are therefore only considering repulsive interactions. Picturing the scattering object to be a sphere, we can posit the existence of a nuclei and spin state only dependant parameter b, called the scattering length. We therefore conjecture that

$$\psi_{sc} = -\frac{b}{r}e^{(ikr)} \tag{4.3}$$

We can imagine b being either real or imaginary. If the scattering length is complex, we can understand this to be the case of absorbtion. Thus, even though we are considering scattering, we can encode absorbtion as well. At present, there is no theory with which to calculate b. All values for b that exist today are experimentally determined.

Let ψ_{inc} be the incident waveform. If v is the velocity of the neutron, then the number of neutrons passing through area dS per second is

$$vdS|\psi_{sc}|^2 = vdS\frac{b^2}{r^2} = vb^2d\Omega \tag{4.4}$$

The incident flux Φ is just

$$\Phi = v|\psi_{inc}|^2 = v \tag{4.5}$$

Therefore

$$\frac{d\sigma}{d\Omega} = \frac{vb^2d\Omega}{\Phi d\Omega} = b^2 \tag{4.6}$$

Thus the total scattering is just

$$\sigma_{tot} = 4\pi b^2 \tag{4.7}$$

This is an important result. The physics of coherent and incoherent scattering is recast in this type of formalism. We will not go into the details here,

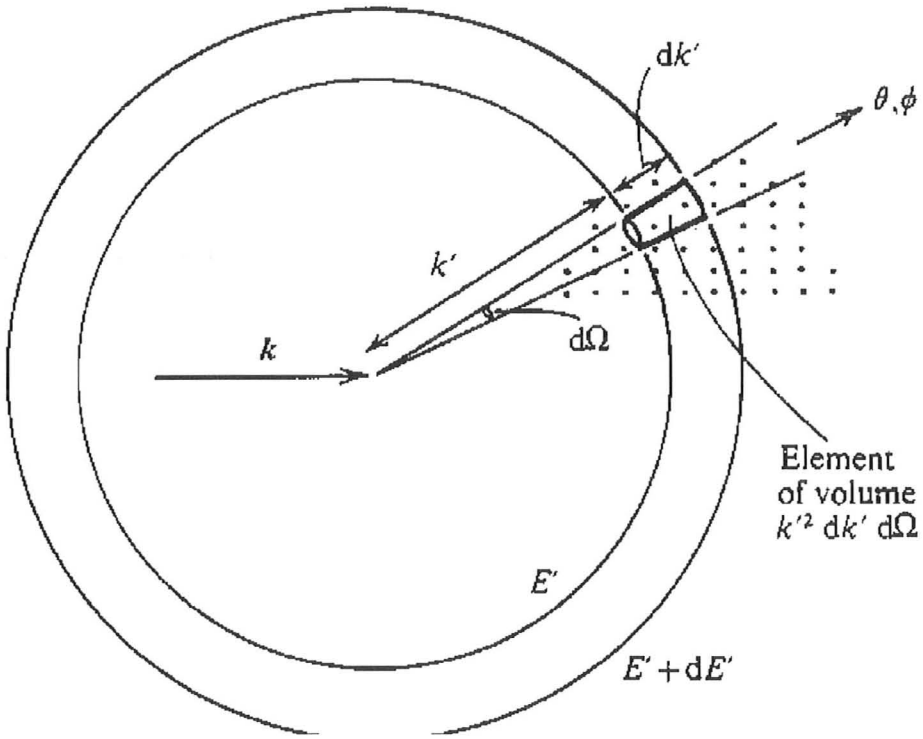

Figure 4.2: A second way to depict the geometry of a scattering experiment. The advantage of this representation is that using the variables defined here, one can derive a more powerful mathematical representation of the scattering cross section. Specifically, this gemoetry can be used to calculate the number of momentum states in $d\Omega$. This quantity is defined as ρ_{k}

as they are not pertinent to this discussion. However, we cover this much of the physics to submit that we can neglect effects that would be introduced were we to not assume the nuclei as point objects. The final result of the analysis will be stated after we consider the general formalism of scattering in general.

Let us recast the scattering geometry as in figure 4.2

Fermi's Golden rule tells us that

$$(\frac{d\sigma}{d\Omega}) = \frac{1}{\Phi d\Omega}\Sigma_{\mathbf{k'}ind\Omega}W_{\mathbf{k},\lambda->\mathbf{k'},\lambda'} \tag{4.8}$$

where W is the number of transitions per second from the initial state to the final state. If we allow the potential of the crystal to be defined as V, then

$$\Sigma_{\mathbf{k'}ind\Omega}W_{\mathbf{k},\lambda->\mathbf{k'},\lambda'} = \frac{2\pi}{\hbar}\rho_{\mathbf{k}}| < \mathbf{k'}\lambda'|V|\mathbf{k}\lambda > |^2 \tag{4.9}$$

Now, we know that we will only have scattering if the change in wavevector is a reciprocal lattice vector. Glossing over the mathematics of normalizing the scattered flux to the incident flux by using a unit cell of the reciprocal lattice:

$$(\frac{d\sigma}{d\Omega})_{\lambda->\lambda'} = \frac{k'}{k}(\frac{m}{2\pi\hbar^2})^2| < \mathbf{k'}\lambda'|V|\mathbf{k}\lambda > |^2 \tag{4.10}$$

Now, we require there be energy conservation in this system. Ergo we can deduce that:

$$(\frac{d\sigma}{d\Omega dE'})_{\lambda->\lambda'} = \frac{k'}{k}(\frac{m}{2\pi\hbar^2})^2| < \mathbf{k'}\lambda'|V|\mathbf{k}\lambda > |^2\delta(E_\lambda + E_{\lambda'} + E - E') \tag{4.11}$$

where E_λ is the energy of a neutron of wavelength λ and E is the energy of the crystal. That is, the partial differential cross section is simply requiring that the energy change in the neutron be accounted for in the energy change of the crystal.

This is the general form of the scattering. By performing Fourier transforms and making a few assumptions, we would eventually find that:

$$(\frac{d\sigma}{d\Omega dE'})_{\lambda->\lambda'} = \frac{\sigma_{coherent}}{4\pi}\frac{k'}{k}\frac{1}{2\pi\hbar}\Sigma_{jl}\int_{-\infty}^{\infty} < e^{(-i\mathbf{K}\bullet\mathbf{R}_l(0))}e^{i\mathbf{K}\bullet\mathbf{R}_j(t))} > e^{-i\omega t}dt \tag{4.12}$$

$$(\frac{d\sigma}{d\Omega dE'})_{\lambda->\lambda'} = \frac{\sigma_{incoherent}}{4\pi}\frac{k'}{k}\frac{1}{2\pi\hbar}\Sigma_{j}\int_{-\infty}^{\infty} < e^{(-i\mathbf{K}\bullet\mathbf{R}_j(0))}e^{i\mathbf{K}\bullet\mathbf{R}_j(t))} > e^{-i\omega t}dt \tag{4.13}$$

where

$$\sigma_{incoherent} = 4\pi(< b >)^2, \sigma_{incoherent} = r\pi(< b^2 > -(< b >)^2) \tag{4.14}$$

Now, we have not reproduced many of the steps taken to arrive at these last three equations. Regardless, there are two main points here. First, the picture of spherically symmetric nuclei re-emerges naturally from the derivation. Second, we have not found any new physics through the derivation. This is still equation 4.11. All that has been done is the potential function V has been developed and we have moved into a particular basis. This is useful for the purposes of interpretation only. Equation 4.11 contains the only points we require to understand nuclear scattering qualitatively: momentum and energy will be conserved. Therefore, our reciprocal space maps that we will produce will be oriented as momentum conservation directs to us what a scattering angle implies, and we know the energy change of the neutron is the energy change in the crystal.

4.4 Magnetic Scattering

Now, because the neutron has a magnetic moment, it can couple to the magnetic moments in a sample system. The operator governing this is

$$\vec{\mu}_n = -\gamma \mu_n \vec{\sigma} \tag{4.15}$$

where $\gamma = 1.913$, $\vec{\mu} \approx \frac{e\hbar}{2m_p}$. This will yield a magnetic potential V_m to interact with the spin state of our system. Now, the magnetic moment of an electron is greater than that of the nucleus, so we will consider only electronic interactions here. Note that the formalism is essentially the same to consider the nuclear moments as well, albeit more cumbersome algebraically. The operator for the electron is

$$\vec{\mu}_e = -\gamma \mu_B \vec{s} \tag{4.16}$$

where we take the spin state of the electrons to be $\vec{s}$. Assume the electron has momentum $\vec{p}$. The Biot-Savart law then gives us

$$V_m = \frac{\mu_0}{4\pi} \gamma \mu_N 2\mu_B \vec{\sigma} \bullet [\nabla \times (\frac{\vec{s} \times \hat{R}}{R^2}) + \frac{1}{\hbar}(\frac{\vec{p} \times \hat{R}}{R^2})] \tag{4.17}$$

Therefore the partial differential cross section for magnetic scattering is:

$$(\frac{d\sigma}{d\Omega dE'})_{\sigma\lambda -> \sigma'\lambda'} = \frac{k'}{k}(\frac{m}{2\pi\hbar^2})^2 | < \mathbf{k'}\sigma'\lambda' | V_m | \mathbf{k}\sigma\lambda > |^2 \delta(E_\lambda - E_{\lambda'} + E - E') \tag{4.18}$$

This last equation can be recast in terms of the scattering vector $\vec{Q}$. However, this is a detailed calculation. We will only state the result here. Before we present the result, we define the energy difference in the crystal $E - E' = \hbar\omega$:

$$(\frac{d\sigma}{d\Omega dE'})_{\sigma\lambda->\sigma'\lambda'} = (\frac{\gamma\mu_0 e^2}{4\pi m_e})^2 \frac{k'}{k} | < \sigma'\lambda'|\vec{\sigma} \bullet \vec{Q_\perp}|\sigma\lambda > |^2 \delta(E_\lambda - E_{\lambda'} + \hbar\omega) \quad (4.19)$$

where

$$\vec{Q_\perp} = \Sigma_i e^{i\mathbf{K}\bullet\mathbf{r}_i}[\hat{\mathbf{K}} \times (\mathbf{s}_i \times \hat{\mathbf{K}} + \frac{i}{\hbar K}(\mathbf{p}_i \times \hat{\mathbf{K}})] \quad (4.20)$$

The important point here is that the magenetic interaction will only occur if the magnetization is perpendicular to the scattering vector. This point can be useful in identifying what interactions can be responsible for a particular kind of scattering in practice.

Full details can be found in [7]

4.5 Experimental Techniques

4.5.1 Introduction

In the lab, for single crystals, there are three kinds of neutron scattering that are employed. We shall only discuss two: the triple axis and time of flight methods. More recently, a number of varients to these techniques have been created, including admixtures of the two techniques. However, we will only consider the two traditional versions of these techniques here.

4.5.2 Triple Axis Instruments

The triple axis spectrometer is of particular pride to Canadians as it was developed by Bertram Brockhouse, a Canadian working at McMaster University. Though in present day, this technique is starting to be, in some regards, overshadowed by its predecessor, the time of flight technique, triple axis spectroscopy remains an essential method in any neutron scattering program.

The technique has a similar design to the rotating anode x-ray machine. A perfect crystal is used to monochromatize a beam of neutrons by reflecting only those neutrons of the correct wavelength. These neutrons then scatter off of a sample crystal. However, we know that unlike in the x-ray case, the change in kinetic of the neutron is significant relative to the initial neutron kinetic energy. Therefore, neutrons that have scattered inelastically can be easily distinguished from those that scattered elastically. This is why a second perfect crystal, called the analyzer crystal, is used to select out neutrons of a second desired wavelength. In this way, this technique can obtain information about reciprocal space, just as a rotating anode machine can, in addition to dynamic information through the use of the second monochromating crystal.

A weakness of this technique is there is no real way to stop the harmonics of the desired neutron energy. To deal with this, various filters can be used depending on the circumstances [22]. However, there is no way to perfectly remove harmonic contamination in this technique.

The last important aspect to the operation of this method is collimation. We seek a monochromatic beam that is well aligned. This is why narrow slits made of neutron absorbing materials are placed in the beam. Thus, only

neutrons whose propogation directions are in a desired direction, to within some angular tolerance, are used.

Let us briefly note the reason for the name of this technique. It is so named because the monochromating crystal, sample crystal, and analyzer crystal can all be rotated. This gives an experimenter control over "three axes" of the experiment: incident wavevector, the scattering potential and the final wavevector to be analyzed.

This method is schematically shown in figure 4.3. Further details can be found in reference [22].

4.5.3 The Time of Flight Technique

A limitation of the triple axis method is only one final neutron energy can be measured at a time, as well as only one scattering vector. But, with the advent of modern computers, one can now time events to fractions of a second as well as amass vast quantities of information simultaneously. This can be exploited by the time of flight technique.

Figure 4.4 displays the schematics of this method. Neutron optics are employed between the source and the apparatus to align the neutron beam. The beam then reaches a series of rotating neutron absorbing materials with holes cut in them. The holes will each be aligned with the neutron beam at different times. If a neutron moves too fast, it may reach the hole of the first material, but not the hole of the second. If a neutron moves too slowly, it will not reach the hole of the first material. Thus, only neutrons moving at

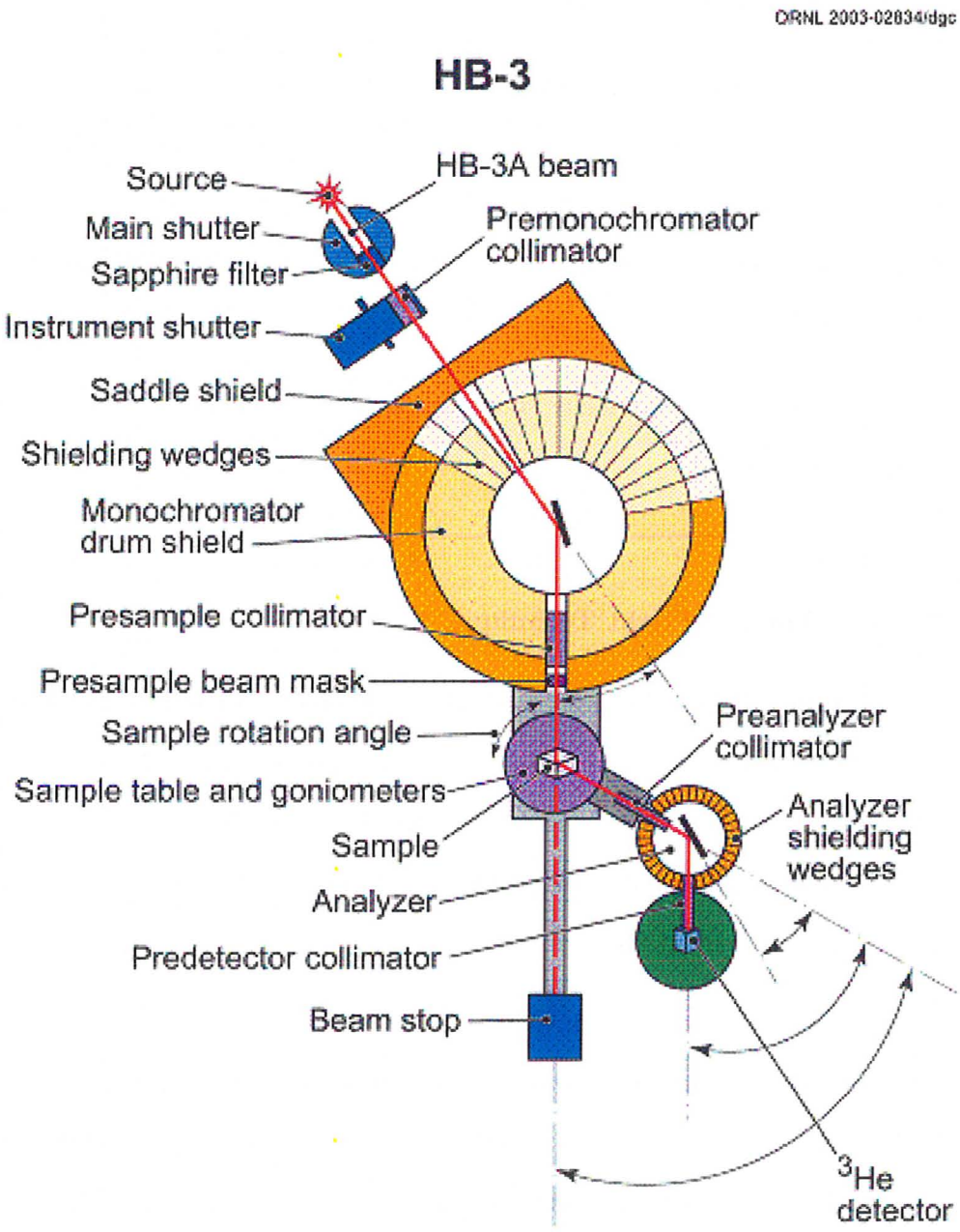

Figure 4.3: Triple axis spectrometer HB3 at Oak Ridge National Labs [8]

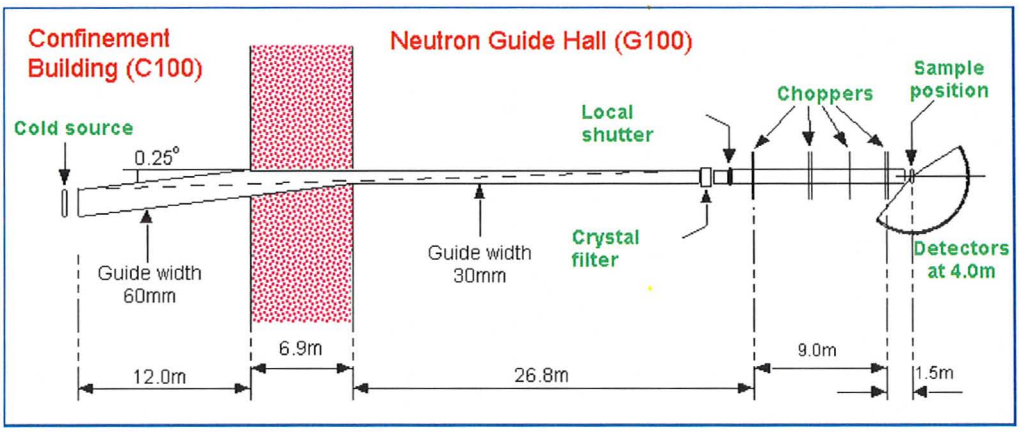

Figure 4.4: The time of flight apparatus used at DCS [9]

a desired velocity will be able to pass through. This is the same idea that is used with traffic lights to help ensure traffic moves at the speed limit. This is how the beam is monochromatized.

The main measurement of this technique is time. Knowing when the hole of the last absorbing material is aligned with the neutron beam defines an initial time t = 0. By then knowing the distance to the sample and the distance from there to the detector by measuring the "time of flight" for the neutron, one is effectively measuring the neutron's velocity and hence its energy.

By then also having a series of detectors placed all the way along a back wall of the machine, one can measure several wavevectors simultaneously. Combined with the previous point, one is also measuring a series of neutron energies at the same time. Therefore, the time of flight technique measures a vast range of reciprocal space and dynamics all at once.

Chapter 5

Prelude to Chapters 6-8: Neutron and X-Ray Scattering Studies of LBCO

The contents of this chapter discuss the neutron scattering results taken on five single crystals of LBCO of dopings x = 0, 0.0125, 0.025, 0.035 and 0.095. The main focus here is on examining the spin dynamics of these systems as the elastic magnetic scattering was well described in a previous thesis [11]. Data considered here were taken at four instruments. The experiments will be grouped based on what aspect of the physics their measurements address: the nuclear structure, low energy dynamic magnetism and the dispersion of the dynamic magnetism.

From examination of the elastic magnetic scattering, a coherent picture that is consistent with previous research, both by our group and in the literature that was discussed in chapter 2, can be achieved. This detailed analysis leads to the phase diagram that will be shown in chapter 7. What should be noted is that this phase diagram predominantly focuses on how the system evolves in doping and temperature space. Chapter 7 will develop more features of the dynamics, not all of which encapsulated in the phase diagram.

Chapter 8 will focus on the magnetic spin dynamics at energy transfers that our greater than were probed by the data in chapter 7. It will be shown that our measurements form a picture that is consistent with results from other related systems. When numerical comparison is possible, we will find quantitative agreement between results for LBCO and those reported in related systems.

The overarching picture is as follows. As was found in the static magneticc case, dynamic scattering measurements reveal that there are two dimensional rods of scattering existing at the same incommensurate wavevectors as the static magnetic rods of scattering. However, the data suggests that in lieu of there being a hard transition to this dynamically correlated state, the spin dynamics are in fact a gapless excitation of the system. There is also evidence for a crossover effect at higher temperatures. The crossover temperature, according to the results of our analysis, seems consistent with the pseudogap temperature; although the evidence acquired to date not conclusive. Furthermore, as was found in the elastic magnetic scattering case, the incommensurability of these rods does increase as a function of doping. Upon increase in neutron energy loss, just as in the case of LSCO [4], an hour glass shaped dispersion is present, with a minimum at approximately 9 meV in x = 0.035.

To explore this, the structure of the remainder of this thesis will be to consider each experiment in turn in an order that is in line with the picture being given here. First, data taken at the ARCS instrument at the SNS combined with rotating anode x-ray diffraction data will be examined for the purpose of given a crystallographic orientation to the system. Next, data taken

at the DCS instrument at NIST will be discussed. A brief review of the elastic magnetic scattering data, as presented in a previous thesis [11], will be given, followed by a discussion of the spin dynamics this data reveals. Following this, data taken at HB3 at HFIR will be considered to establish the existence of the resonance and explore the lower energy physics of this system. To conclude, a brief survey of some preliminary SEQUOIA results will explore how the incommensuration of the system evolves at energies above the resonance. The contents of chapter 7 and the HFIR data from chapter 8 are in preparation for publication and the remaining data in chapter 8 is still in the process of being analyzed.

Chapter 6

ARCS and Rotating Anode X-Ray Studies of Structural Features at $(\frac{1}{2}, \frac{1}{2}, L)$ positions in LBCO

6.1 Introduction

The purpose of this experiment was to explore the Bragg peaks found at $(\frac{1}{2}, \frac{1}{2}, L)$ positions in a superconducting x=0.095 sample, where L is an integer. At the time of the experiment, these peaks were of unknown origin and were not anticipated. By the conclusion of this analysis, it will be clear that these are structural peaks. Originally, this experiment was chosen as a commissioning single crystal experiment for the ARCS spectrometer. In this spirit, we shall proceed as though these features were unknown.

The first interesting point is that these signals are only at integer L. This is in contrast to the rods of scattering that were investigated previously [11], which are isotropic in L. Given the signal strength and restrictions on reciprocal space locations, this shows that these signals are three dimensional correlations

of some sort and are a phase that coexists with the rods of scattering. Further, since for x = 0.095 we know T_N is around 30K, then perhaps these signals are structural.

The experimental details are as follows. A sample of x = 0.095 LBCO was mounted in a ^4He closed cycle refrigerator. The experiment was carried out using tetragonal unit cell notation. The chosen crystal orientation for this experiment was the (HK0) plane. During the experiment, three temperatures were measured: 5K (base temperature), 50K and 297K. The incident beam energy was 60 meV and was selected by using a Fermi chopper rotation frequency of 480Hz with count times of approximately 10-15 minutes. Neutron fluxes were normalized to the proton charge incident on the SNS mercury target that produces the neutrons used in the experiment. The angles measured ranged a total of approximately 40^o in 3^o steps.

6.2 Neutron Measurements

Figure 6.1 shows two representative slices of the diffraction data. It is binned over all L collected. They are raw data sets at base temperature and room temperature. As can be seen at base temperature, there is a peak at all $(\frac{1}{2}, \frac{1}{2}, L)$ positions. Note, we are not in the three dimensional magnetically ordered region of the cuprate phase diagram [3]. We note that by room temperature, these peaks disappear. Natural questions to ask here are: Are these peaks structural or magnetic? What is their dimensionality?

Let us first address the question of signal dimensionality. The conclusion of Braggs law is that a three dimensionally ordered state will yield intense Bragg

spots in all directions. In figure 6.2 we find these features appear as spots in two orthogonal planes. These data demonstrate that the $(\frac{1}{2}, \frac{1}{2}, L)$ peaks are three dimensional.

The temperature dependence of these $(\frac{1}{2}, \frac{1}{2}, L)$ peaks are demonstrated in figure 6.3. This figures displays cuts along the H direction. These cuts are binned such that -1.7 $\leq K \leq$ -1.3 R.L.U. This range guarantees that a cut along the H direction will yield $(\frac{1}{2}, \frac{1}{2}, L)$ type information. All L are integrated together here. Three cuts are displayed: one for each temperature. Notice that at integer H there seems to be no temperature dependence. However, at half integer H, the peaks disappear in the room temperature data set. Recalling that T_N in this system is around 30K, these peaks are likely structural in nature. However, we cannot confirm this assertion from this information alone.

Let us turn now to the L dependence of these features. Figure 6.4 is a series of cuts through the data. The H and K range used are the same as in Figure 6.3. However, now L are integrated about a narrow region about each integer L value. The 297 K data set was taken to be a background for this figure. This is because we are interested in features at half integer positions, which only exist below 297K. As can be seen, peaks at all half integer H appear for all L. Note that there is a symmetry to the signal strength between positive and negative L. This offers a complete survey of the structure of these features. However, this data alone cannot address the origin of these signals.

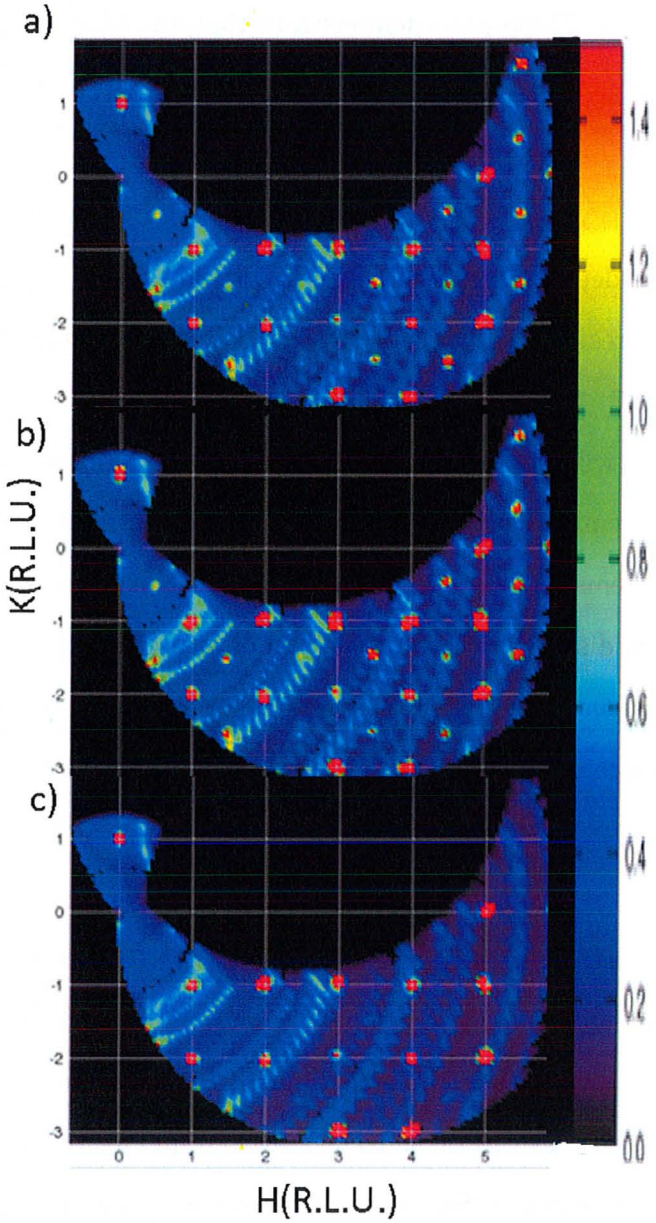

Figure 6.1: Diffraction maps at a) 5K, b) 50K and c) 297K showing that the $(\frac{1}{2}, \frac{1}{2}, L)$ peaks disappear somewhere between 50 and 297K in x = 0.095. These data are all raw data files with no background subtraction. All L have been integrated together

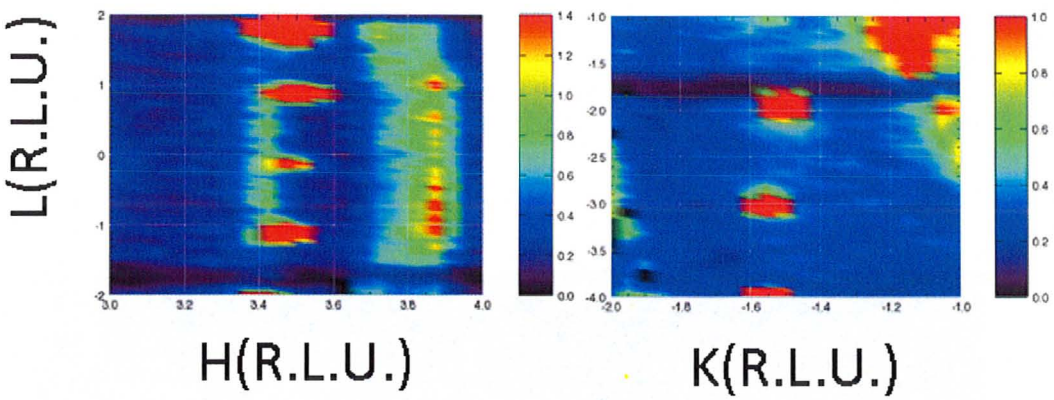

Figure 6.2: T = 5K maps of the HL ($-1.6 \leq K \leq -1.4$), shown on left, and KL ($1.4 \leq H \leq 1.6$), shown on right, planes in x = 0.095. Each map has orthogonal axis integration such that $(\frac{1}{2}, \frac{1}{2})$ type positions are shown. The two maps are of planes that are orthogonal to each other.

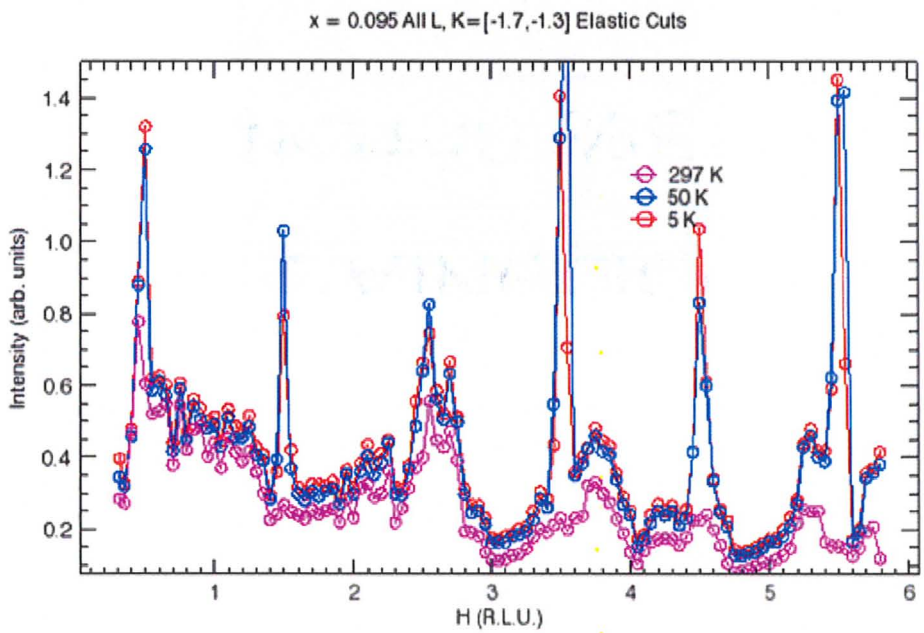

Figure 6.3: Cuts along H with half integer K at all three temperatures. Notice that for the $(\frac{1}{2}, \frac{1}{2}, L)$ features, there is only non-zero signal intensity for the lower temperature data sets. There appears to be no temperature structure to the scattering at these two temperatures.

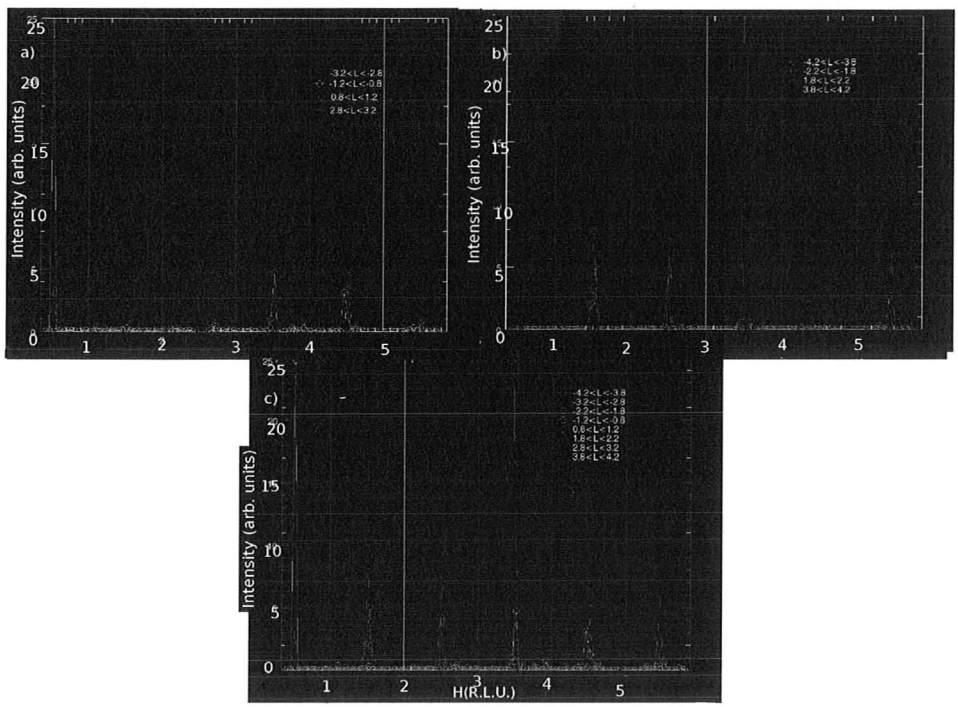

Figure 6.4: Cuts through the $(\frac{1}{2}, \frac{1}{2}, L)$ peaks for a series of different L values centered at $-1.6 \leq K \leq -1.4$. a) has odd L values, b) has even odd values and c) has all L values displayed at once. Note that there is symmetry between positive and negative L values. All L bins are 0.4 R.L.U. wide. This demonstrates the form factor for these peaks.

6.3 X-Ray Measurements

To determine if these features are structural, an x-ray experiment was performed on the four circle diffractometer at McMaster. A single crystal cut from the same crystal measured in the neutron measurements at ARCS was attached to the cold finger of a ^4He closed cycle refrigerator and mounted in reflection geometry. Cu $K_{\alpha 1}(\lambda = 1.54041\mathring{A})$ radiation was selected using a germanium (111) single crystal. The experiment was carried out in tetragonal notation and aligned in the (HK0) plane.

The main features of the data are summed up in figure 6.5. Clearly, as the features can be seen with x-rays, these peaks are structural in nature. We therefore turn our attention to understanding the temperature dependence of the crystal structure. Consider first panel b) of figure 6.5. It shows that there are two transition temperatures in the sample at approximately 275 K and 50 K, which is consistent with the arcs data set. Realignment tests were performed as well to ensure that the low temperature physics, which is where thermal expansion will have the largest effect, was indeed accurate. Turning our attention to panel a) we find an order parameter measurement. We take the scattered intensity to be the order parameter here. Comparison of this measurement to the structural peaks from the parent compound LCO yields excellent agreement. Further, it is found that the structure of LSCO is similar [23]. This confirms that these peaks are structural and are due to the parent compound structure.

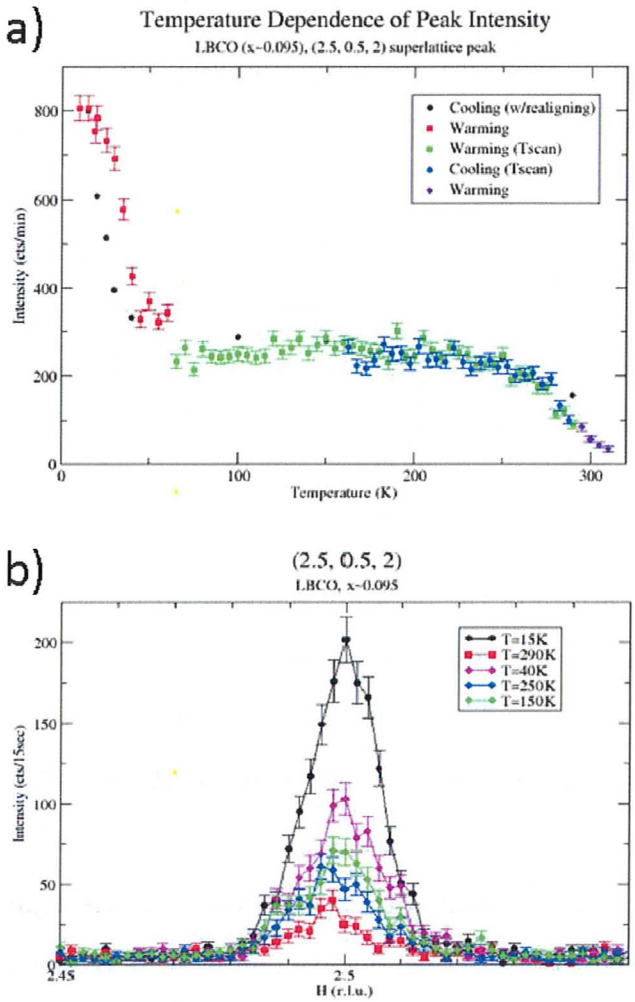

Figure 6.5: X-Ray measurements of x = 0.095 LBCO. a) an order parameter type measurement of intensity vs. temperature. This observation was made twice. Once with alignment at intermediate temperatures and one with a base temperature alignment. These two observations display the same qualitative physics: namely a transition around 50K. b) a series of cuts along the H direction at various different temperatures. There is clearly a reduction in intensity with temperature. However, the peak width remains consistent throughout all temperatures observed.

6.4 Conclusions

From our neutron and x-ray measurements, combined with literature research, we know that these peaks are structural. Through order parameter measurements, we have elucidated their temperature dependence thoroughly. There appear to be two structural transitions: one at 50K and one at 275K. These temperatures do not coincide with those made of the unit cell [24]. However, they have been observed in the parent compound crystal structure.

The main result of this work is that we have confirmation that the data from ARCS appears accurate and hence, our commissioning of the instrument was successful. This experiment also offers insight into how to orient oneself in this system. This an important feature to keep in mind when studying magnetic diffraction in this system as both features occupy the same HK values.

Chapter 7

DCS Time of Flight Experiment on Doping and Temperature Dependence of Two Dimensional Incommensurate Dynamic Correlations in LBCO

7.1 Introduction

From measurements taken at Chalk River [11], it was known at x = 0.0125 that spectral weight from the three dimensionally ordered antiferromagnetic peak was being transferred to some other magnetic feature. The main intent of this DCS experiment was to definitively show that it was due to the onset of a coexistence between two dimensional and three dimensional static magnetism. The experiment was performed at a time of flight spectrometer called DCS. DCS uses a reactor based cold source, so only low energy neutrons are accessible.An advantage of this choice is that it narrows the range of Q viewable. As aluminum powder lines occupy Q in excess of a half integer in the HH

direction by using we can get a clean view of the elastic scattering. This choice also offers high energy and Q resolution, which is useful for studies of low lying excitations in the system. As will be clear in chapter 8, when considering the spin dynamics in this system, one requires the highest possible Q resolution. Therefore, a cold source is advantageous in a number of different ways.

What was found was a signal that had properties in agreement with those found in LSCO. The two dimensional dynamic magnetism, or dynamic rod, was energy independent over the energy range measured, incommensurate, occupied the same position as the static magnetism and even showed the same doping dependence as the static magnetism. This result allows us to perform a detailed analysis of the spin dynamics of this system.

The experiment was carried out on the DCS spectrometer at NIST. DCS is a high energy resolution, time of flight spectrometer. The samples were each mounted in an ILL orange cryostat. The experiment was carried out in tetragonal notation and aligned in the HHL plane. The incident neutrons had a wavelength of 5 $\AA$. Four samples were measured: x = 0, 0.0125, 0.025 and 0.035. x = 0 was measured at the base temperature (1.5K), 35 K and 297 K. x = 0.0125 was measured at 1.5K, 10K, 15K, 20K, 22.5K, 25K, 30K, 35K, 160 K and 297K. x = 0.025 was measured at 1.5K and 35K. Lastly, x = 0.035 was measured at 1.5K, 10K, 15K, 20K, 25K, 30K and 35K.

As described in an earlier thesis [11], combining the data taken in this DCS experiment with order parameter measurements from HFIR and Chalk River yield most of the phase diagram presented in figure 7.1. This phase diagram

encodes nearly all that we know about the static magnetism in the LBCO system over a wide range of Ba dopings.

7.2 Preliminaries

Now, as discussed in chapter 4, a strength of the time of flight technique is that it gives information on both the static and the dynamic magnetism of a system in a single measurement. As a result, in this experiment the low energy physics (1.5 meV or less) were obtained. In addition, during these measurements, the low temperature (less than 35K) physics were well explored in this doping range. A selection of high temperature measurements were also made. Ellucidating the higher temperature regions of the phase diagram is a work in progress.

These rods do not appear to have any energy dependence, as can be seen in figure 7.2. This is confirmed by looking at a cut along the rod. Note that such a cut involves integrating the signal from 0.45 to 0.55 R.L.U. in the HH direction and cutting along the E direction of figure 7.2. The result of this cut is shown in figure 7.3. There is no signal clearly above background within error.

Let us now note the position of this dynamic magnetic rod. It is found occupying the $(\frac{1}{2}, \frac{1}{2}, L)$ position of reciprocal space. Figure 7.4 shows two slices: one of the static magnetic rod in x = 0.025 and one of the dynamic magnetic rod. As can be seen, the two features are similar in their extent and the positions they occupy in reciprocal space. It should also be noted that

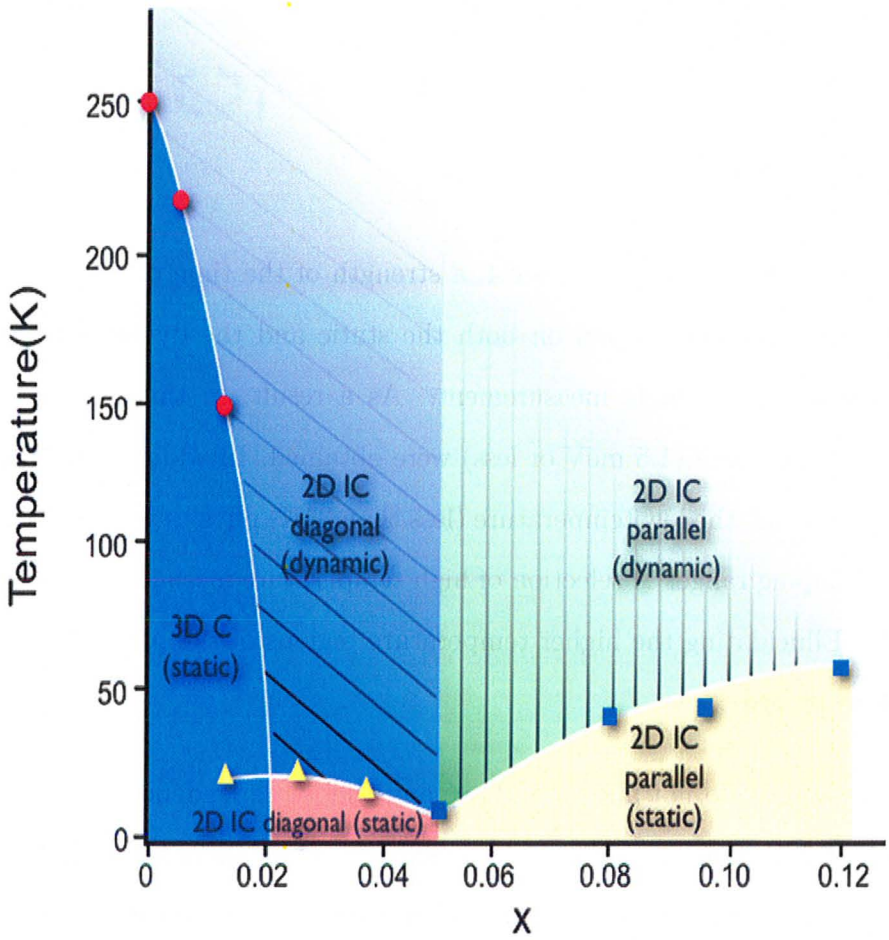

Figure 7.1: Magnetic phase diagram for LBCO as determined by order parameter and diffraction measurements on various LBCO crystals [10, 11, 12]. It shows that upon introductino of holes, the three dimensional commensurate static magnetic state is extinguished by x = 0.02. Also present is a lower temperature incommensurate static incommensurate magnetic state. This state is diagonal with respect to the tetragonal unit cell. At x = 0.05, the magnetism rotates and becomes parallel with respect to the tetragonal unit cell. We also see two dimensional dynamic diagonal incommensurate magnetism at nearly all places in the phase diagram that have been measured for $x \leq 0.035$. Only for x = 0 below 300K has there been no observation to date of a dynamic magnetic signal, though as will be explained there is likely a weak signal there that has yet to be seen.

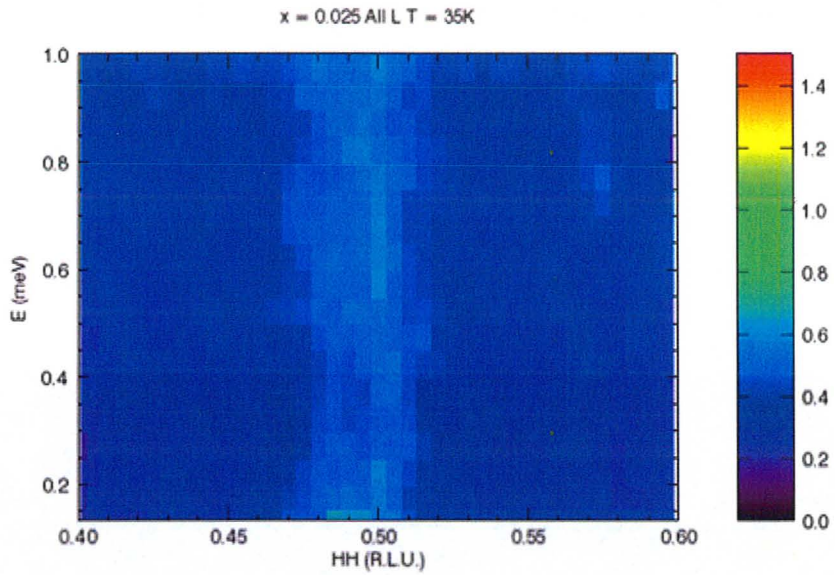

Figure 7.2: Inelastic scattering in x = 0.025. This feature is integrated over all L and is shown at 35K. The focus of this plot is on the dynamic magnetic rod and how it varies with excitation energy.

we have clear evidence that these dynamic correlations are two dimensional in their nature.

7.3 Doping Dependence

The first parameter to address is the doping dependence. The salient point of interest here can best be elucidated in figure 7.5. Here we see the x = 0.035 signal alone followed by a comparison of all signals for $x \geq 0$ (no signal in x = 0 could be seen). Notice that the x = 0.035 data seems consistent with there being a two peaked structure. From the litterature in LSCO [4], one would expect that there be two identical incommensurate peaks if one were to scan along [HH]. This picture is complicated due to crystal twinning. Twinning here

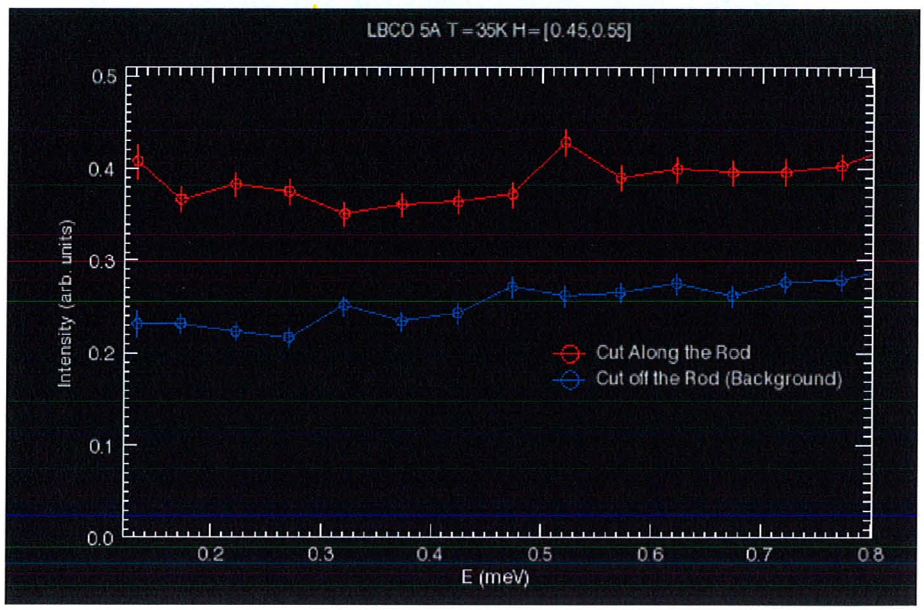

Figure 7.3: Cut along the rod of scattering in E for x = 0.025 and a cut through the background. This is equivalent to line scans parallel to the rod shown in figure 7.2. These clearly demomnstrate there is no concrete evidence for any real energy dependence to the scattering seen here.

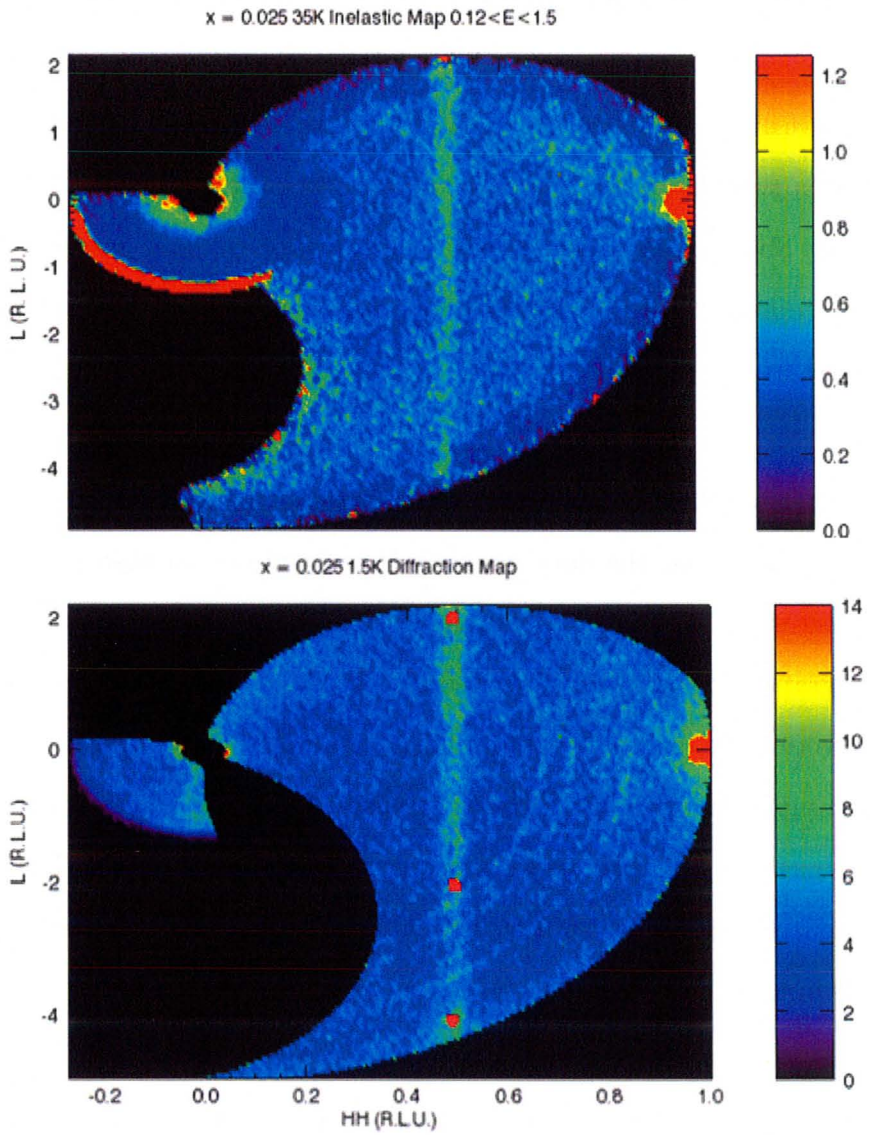

Figure 7.4: a) inelastic DCS data from x = 0.025. b) diffraction map of the same sample. Note that the Bragg spots in b) are in fact structural peaks and not magnetic. Comparision of these panels reveals that the two dimensional dynamic correlations and the two dimensional static magnetic order in this system are qualitatively the same. Note that the reduced intensities for all L below -2 R.L.U. is due to absorbtion by the crystal. These maps are produced by observing the scattering at various different sample rotation angles. Hence some angles require scattering neutrons traverse more sample than others.

is due to the orthorhombicity of this crystal. As the two lattice parameters are not quite equal, at certain unit cell boundaries, there is a mismatch of the the two unit cells. This leads to a twist in the crystal structure, which manifests itself as a twinned peak. Therefore, here we would expect to see four signals in total. Since a spectrometer would be expected to catch slightly off angle features differently, we would therefore expect to see two peaks of different intensity, as we observed.

Supporting this reasoning is the robustness of this feature. Recall that for L$\leq$-1.9 R.L.U. that the data intensity is reduced due to absorption. It was hence checked if restricting the L range would alter the signal shape. Variation in integration step size was also used to ensure that the analysis program was not affecting the quality of the results. The conclusion was that the two peak shaped signal was a robust effect. It seems at this point unlikely that the x = 0.035 signal can be explained well using a signal peak hypothesis. Therefore, it is submitted that the x = 0.035 signal is in fact a sign of two incommensurate signals in the data.

This conclusion lends itself to a natural interpretation of the data in panel b) figure 7.5. Notice that the net feature width increases monotonically with doping. It seems obvious to deduce from this that the incommensuration of the two peaked structure increases with doping. Indeed, the x = 0.025 data set is nearly consistent with in fact being two peaks that are spaced in close proximity to each other. This interpretation lends itself well to explaining the strange depression within the overall peak shape. Given all this evidence, it

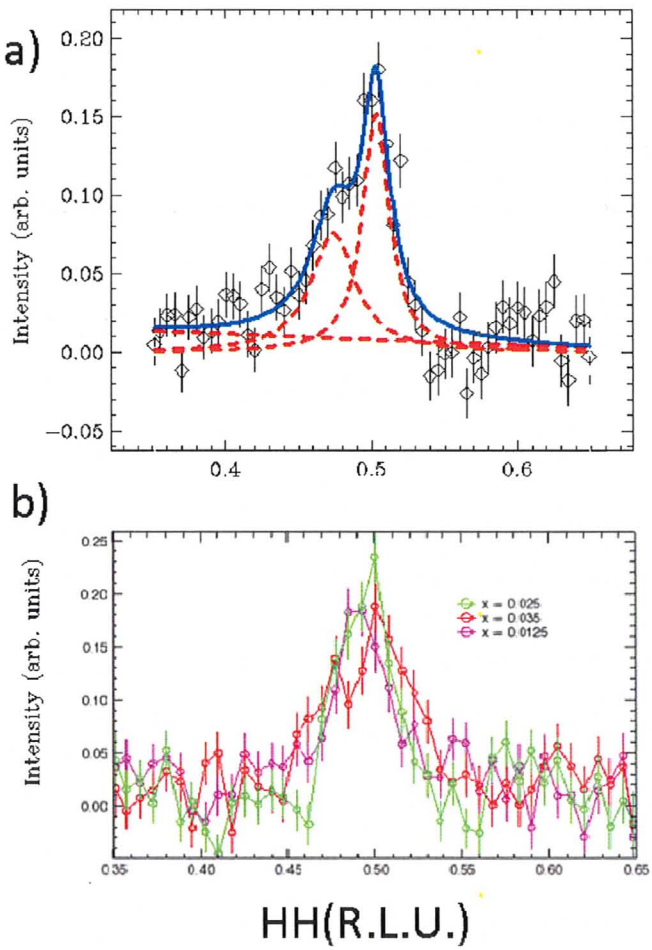

Figure 7.5: Inelastic data taken from DCS. Energies were binned from 0.6 to 1 meV. The reason for this choice was cleanliness of the signal in these regions.a) x = 0.035 35K data. The data is fit two two Lorentzian line shapes. The quality of the fit demonstrates the strength of the two peaked structure hypothesis. b) inelastic scattering from all samples except x = 0. Note that as doping decreases, the width of the half integer HH signal reduces. This is consistent with a two peaked structure where the peak separation increaes as a function of doping.

can therefore be said with confidence that this is evidence in support of the incommensurate two peak hypothesis.

This result is consistent with the litterature[4]. The main difference in the case of LSCO to this aspect of our study is that one can apply gradient pressure annealing to remove the twinning effect in the crystal. Attempts to perform similar techniques to LBCO have been unsuccessful. Hence, the angular allowance of the spectrometer does not add other signals to the periment when working with LSCO. This enables an increase in resolution, which can be used to distinguish two incommensurate signals being sought here. As to the present research, as two distinct peaks can only be seen in x = 0.035, we cannot comment on how the correlation lengths of the two dimensional magnetism evolves in these systems.

Nevertheless, we can make some progress on the x = 0.035 data. Now, one could attempt a resolution convolution analysis to examine the data. Disregarding the details, this method suggests that a given peak is in fact a superposition of resolution function and a signal function. This necessitates that the signal function be narrower than the peak itself. However, fitting the x = 0.035 peak with two lorentzians and a linear background yields that the peaks are on the order of 0.03 R.L.U. wide. Since the correlation length would go as roughly $\frac{1}{\frac{2\pi HalfWidthHalfMaximum}{q}}$, and assuming this overestimate of the signal peak width is accurate, the correlation length is on the order of 56$\mathring{A}$. This value for the dynamic correlation length is in accord with the litterature for LSCO of the same x value [3]. Given the already high correlation of LBCO and LSCO results, it is unlikely a more detailed analysis will change this picture.

Let us now turn our attention to the parent compound. The litterature on LSCO [3] suggests that within the three dimensionally correlated static magnetic region of the phase diagram that the incommensuration of the dynamic magnetic correlations remains fixed throughout this region. It is also suggested that there is no two dimensional signal in the parent compound. However, looking at the inelastic scattering in this systems allows us to posit that instead, there is a two dimensional signal with 0 incommensuration in LBCO. To do this, we must consider that the three dimensional magnetism is a static effect only. It does not evolve with temperature into another ordered state at the same wave vector. However, we know there is a two dimensional signal at higher temperatures at the same wave vector. Though we shall leave the temperature dependence to the next subsection of this chapter, we can still learn about x = 0 rods by going to higher temperatures.

Let us assume there is an x = 0 signal. We know if there is, it must be weak as we do not see it at low temperatures. However, suppose the dynamic susceptability drops off with temperature slowly. At low energies, a change in temperature can result in drastic changes in the Bose factor, which we will discuss in detail later. For now, we will note that at 1 meV, the Bose factor is approximately 200 times larger at 300K than at 1.5K. Figure 7.6 is a view of the raw scattering at 300K. It can clearly be seen that there is a weak rod at the usual $(\frac{1}{2}, \frac{1}{2}, L)$ position. The evidence for the existence of a rod at lower temperatures is more difficult to justify. If the signal is there, it is simply too weak to pull out with the counting times we used. However, when we come to the temperature dependence, there does seem to be evidence to motivate the

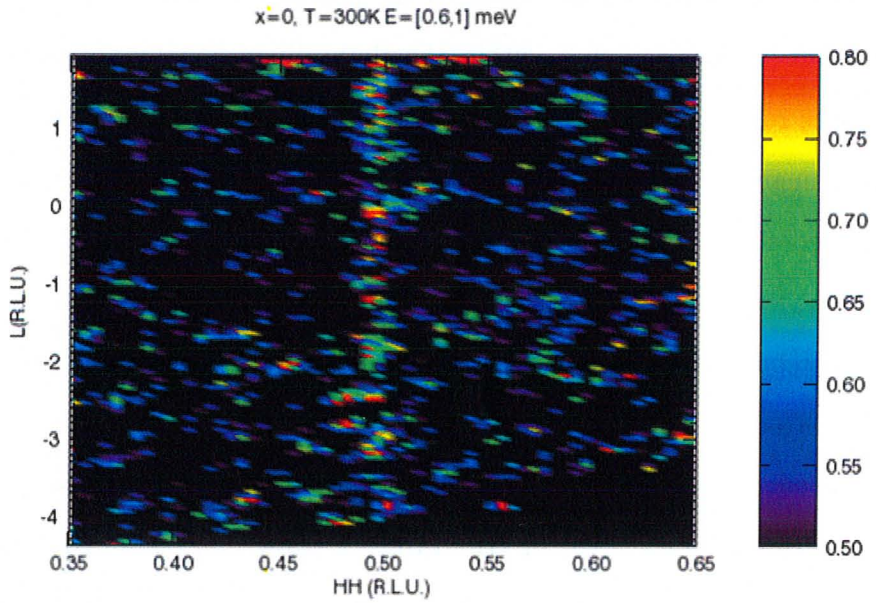

Figure 7.6: Inelastic scattering in x = 0. Note that this rod is qualitatively narrower than the same signals in in previous figures. This observation is in line with the assertion that the incommensuration continues to decrease doping inside the three dimensional commensurate magnetically ordered region of the phase diagram. The data is integrated over $0.6 \leq E \leq 1$ meV to show the cleanest image possible.

picture that there is a signal at lower temperatures in x = 0 and it is simply a weak one.

7.4 Temperature Dependence

Figure 7.7 gives insight into how the scattering evolves as a function of temperature. It shows the scattering in both x = 0.0125 and 0.035. Clearly, the scattering is increasing in intensity. Indeed, as is seen in figure 7.8, the story is unchanged by looking at the temperature evolution of the energy dependence. The scattering in these latter figures appear to originate from lower Q and

start extending to higher energies. At first glance, this suggests that as the static magnetic rods dimminish, the scattering instead becomes dynamically correlated. Naively, this makes sense given that the two features occupy the same position in Q space and indeed it appears as the static magnetic rods vanish, the dynamically correlated rods may well intensify.

However, this interpretation is incorrect. True, it appears that the inelastic features are intensifying with temperature. However, we must not forget that

$$S(Q,\omega) = \chi(Q,\omega) f(T,\omega) \tag{7.1}$$

where f is the Bose factor. Remember, the Bose factor is a factor that encodes population due to thermal effects. We write

$$f(T,\omega) = \frac{1}{1 - e^{-\hbar\omega/k_B T}} \tag{7.2}$$

Notice that as ω goes to 0, the Bose factor increases. Further, as T tends to infinity again the Bose factor increases. As was discussed earlier, for an energy transfer of 1meV, in going from 1.5K to 300K is a factor of 200 increase in the Bose factor. Therefore, to correctly identify magnetic effects requires one to remove the influence of the Bose factor. This is shown in figure 7.9. Assuming an empty can background subtraction is sufficient to remove all background in our signal, simply dividing the inelastic scattering data by the Bose factor will yield the dynamic susceptability. Ideally, one would use data taken of the sample when there is no signal present to eliminate the background. However, as we cannot be sure any temperature data set is truly signal-free, this kind of

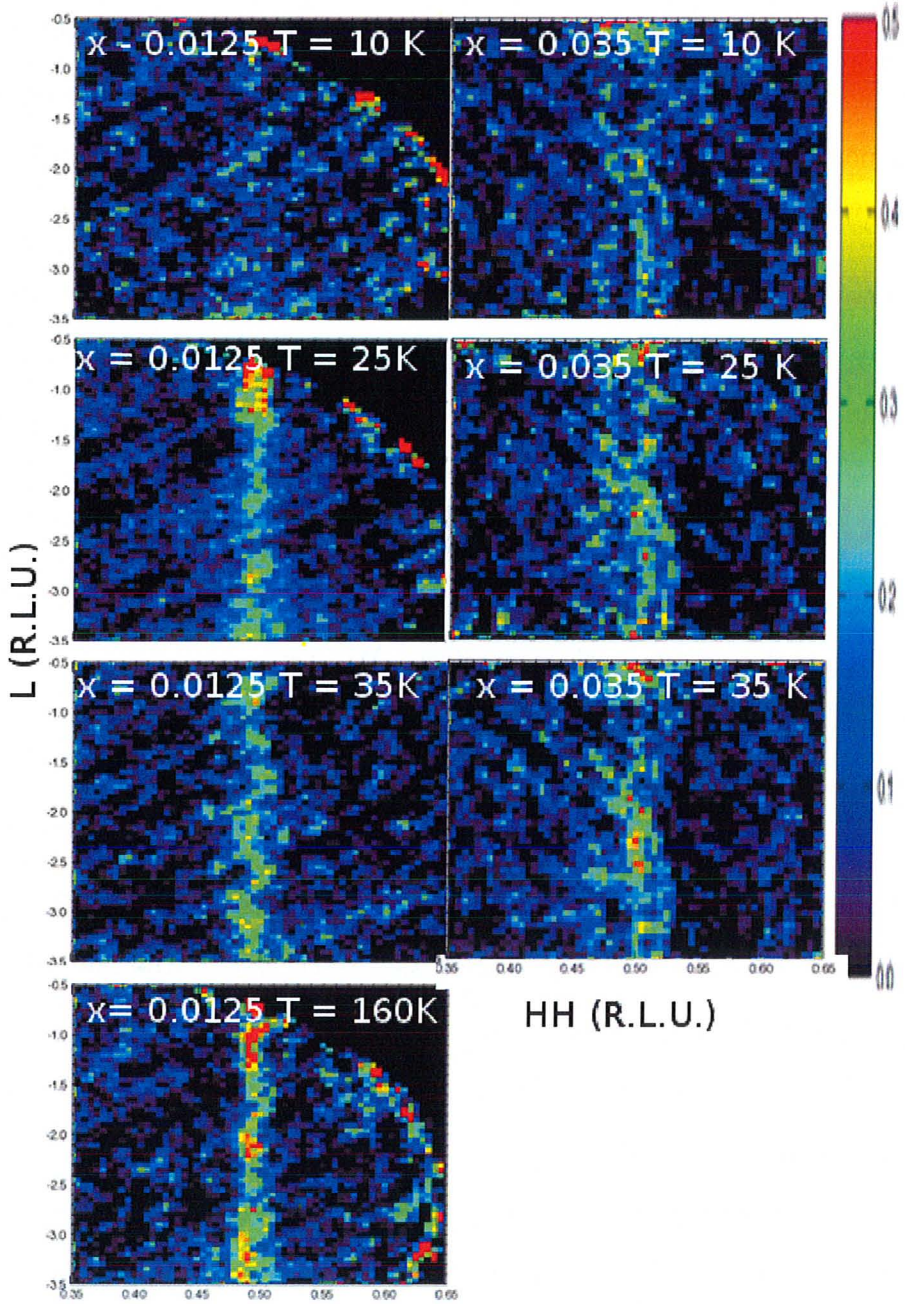

Figure 7.7: Inelastic scattering in x = 0.0125 (left) and 0.035 (right). The top figures are at 10K and ascend to 160K (fox x = 0.0125) or 35K (for x = 0.035). Empty can background subtractions were performed, with $0.12 \leq E \leq 1$ meV.

subtraction cannot be done. We are also further assuming that the resolution function is negligible when compared to the width of our signal. Otherwise, in truth we should perform this analsis after a resolution convolution. However, we suspect from the elastic scattering that the resolution function is that this assumption is valid.

Let us now consider the data in figure 7.9. Here we have evidence that the dynamic susceptibility is decreasing as a function of temperature. Panel a) clearly shows that as a function of temperature we have a reduction in the peak intensity of the dynamic signal. Furthermore, panel b) shows the net intensity of thc rod of scattering. To produce this panel, a more complex form of analysis was used. Rather than fitting all of the data with the naieve background subtractions we have used thus far, to ensure the background is properly understood, the following procedure was used. We know that there is no significant source of constructively interfering scattering except for that due to the dynamic magnetism. After performing a cut along the HH direction, a region that we know the dynamic magnetism occupies is removed. This region is the $0.45 \leq HH \leq 0.55$ R.L.U. Elimination of this portion of the data will leave a constant signal for the remaining Q positions, which we take to be the background. region of the cut. We therefore perform a sloping linear fit of this background. The result of this analysis is then used for background subtraction. As an additional precaution, we once again use the restricted energy range $0.6 \leq E \leq 1$, which is the energy range with the cleanest section of the signal. Upon performing this analysis, what is clear is that the magnetism is strongest at lower temperatures.

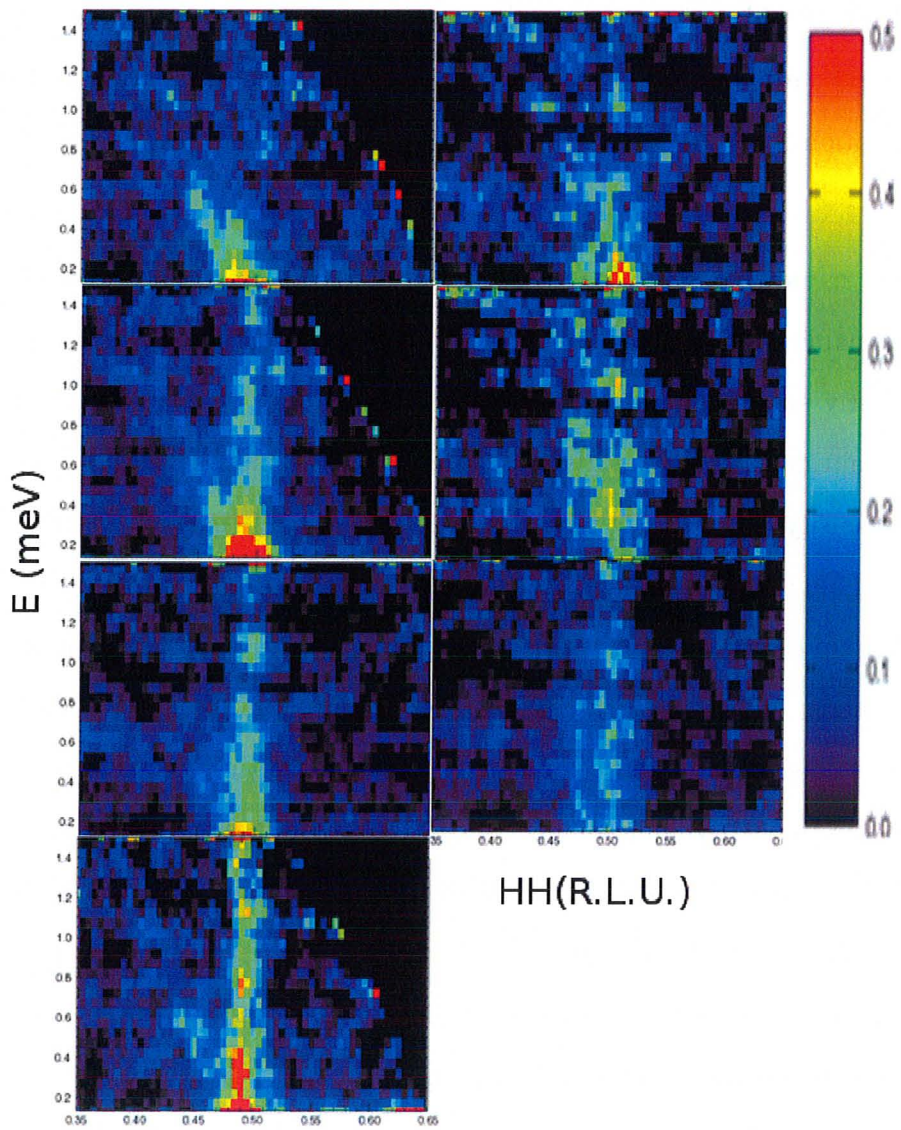

Figure 7.8: Energy vs. Q dependence of the dynamic rods in x = 0.0125. All L are integrated over and an empty can background is subtracted. Notice that the features seem to emenate from the lowest energies displayed.

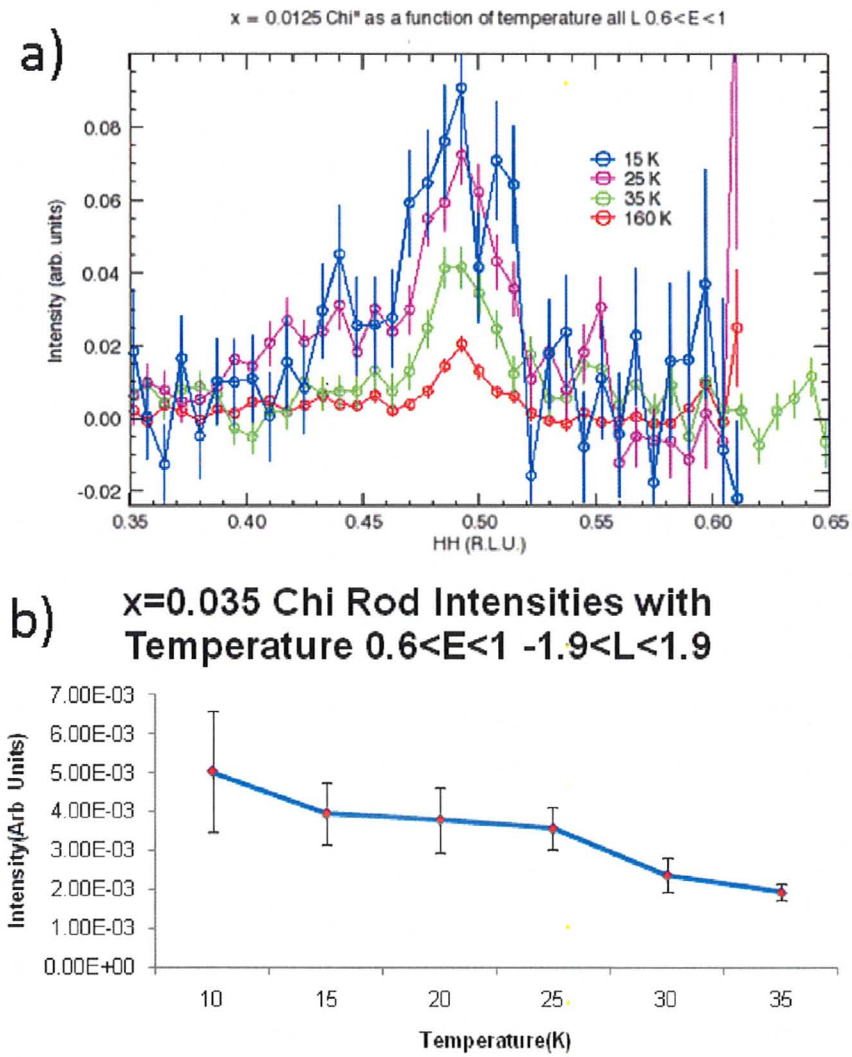

Figure 7.9: a) Dynamic susceptibility as a function of HH at various temperature in x = 0.0125. b) Total dynamic susceptibility $0.35 \leq HH \leq 0.65$ R.L.U. in x = 0.035. This is made by integrating the dynamic magnetic signals in x = 0.035, which appear as similar to the cuts shown in panel a), and background subtracted by the more sophisticated analysis discussed in the text. The result of these plots is clear demonstration of the strength of the dynamic magnetic correlations is diminishing with temperature.

We also have insight into some of the dispersion in this system given this data set. Implicit in the previous quantitative analysis is that the incommensuration of the dynamic correlationsremains constant. However, figure 7.10 shows otherwise. Looking at the inelastic scattering as a function of temperature, it is clear that the peak is narrowing. This shows that the incommensuration must be reducing as a function of temperature. Therefore, the measured intensity at the rod position will appear even more intense, as it is the superposition of two features that are approaching occupying the same Q position. Therefore, figure 7.9 is also an overestimation of the dynamic susceptibility as a function of temperature. The real susceptibility as a function of temperature is in fact lower than what was plotted. We have therefore shown that there is some slight dispersion to our signal that is usually not observable in our data due to limitations in resolution. We have also demonstrated that the results of the analysis in figure 7.9 is robust.

To end the results section for this experiment, let us discuss a final aspect of the data that is not yet conclusive. Notice that in figure 7.1, the dynamic correlation regions of the phase diagram fade to white at higher temperatures. The temperature at which the colour disappears is around the temperature T* for the pseudogap. The reason it appears as though we are suggesting that the dynamic correlations become nearly negligible at the pseudogap is because our data suggests that there is a crossover in the scattering at T*. Consider figure 7.6. This is a figure showing the existence of a rod at 300 K in the x = 0 compound. Now consider figure 7.9. We know that the dynamic susceptibility tends towards 0 in x = 0.0125 by 160 K from this plot. Lastly, consider figure 7.11.

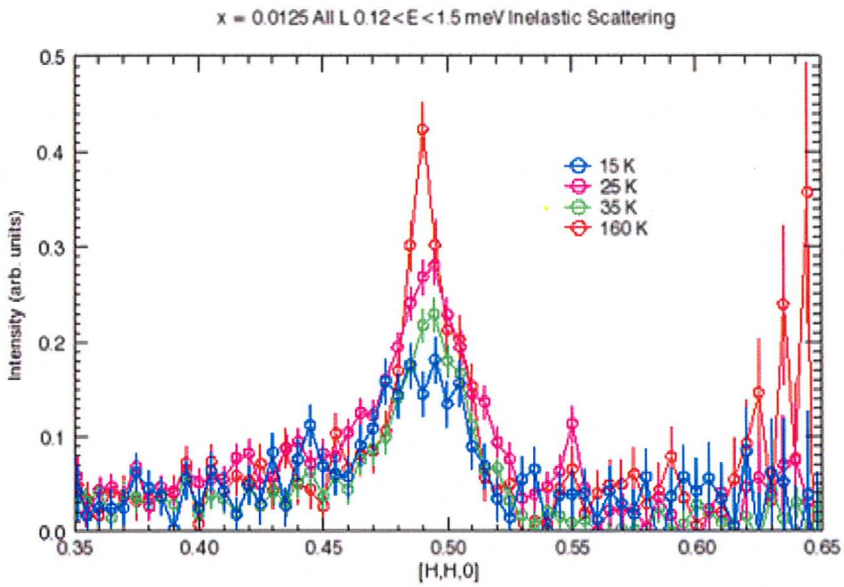

Figure 7.10: Inelastic scattering plotted for four temperatures in x = 0.0125.

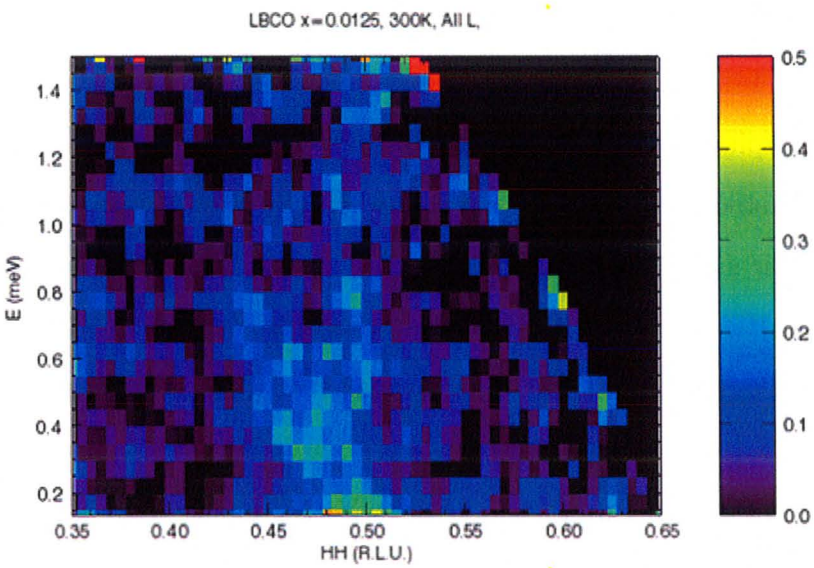

Figure 7.11: Inelastic scattering at 300 K in x = 0.0125

Notice that there is a spurious feature for E $\leq$ 0.6 meV. However, unless one knew there was additionaly a dynamic magnetic rod of scattering there, it would be impossible to convince oneself of its existence from this data alone. All cuts through this data set yield the same null result. It is submitted if a long experiment were performed at this temperature, a weak feature would eventually be seen. Combining all this information: dynamic magnetic rods of scattering persist in x = 0 to 300 K, dynamic magnetic intensities decrease with temperature in spite of an increase in commensuration, and seeing as there is no evidence of a dynamic magnetic correlation at 300 K in x = 0.0125, we conjecture that there is some crossover temperature for our dynamic correlations. We further believe this crossover temperature to be consistent with that of T*.

7.5 Conclusions

The doping dependence of the spin dynamic correlations in LBCO are well understood. We observe along the HH direction a two peak structure that is split symmetrically about the $(\frac{1}{2}, \frac{1}{2})$ position. As the magnetism lies along the HH direction, it is therefore diagonal magnetism with respect to the crystallographic unit cell. This is consistent with previous studies of this system [10] [24]. We have also observed that there is an increase in peak splitting in this structure that increases with Ba doping. Again, this has been seen in the litterature [4].

However, the temperature dependence is not well understood yet. What seems clear is that we have a gapless, energy independent excitation whose in-

commensurate structure becomes increasingly commensurate with an increase in temperature. We also know that the dynamic magnetism is strongest at low temperatures. However, we have only probed low energies with this data and we only have a few high temperature data points. However, what we have seen thus far seems consistent with an apparent cross over at a temperature similar to the transition temperature for the pseudogap. What we have conclusively seen though is that the incommensuration of our signal's two peaked structure decreaes with temperature.

Chapter 8

Dispersion of Spin Excitations in LBCO

8.1 Introduction

In the last chapter, we explored two axes of the parameter space of the dynamic magnetic rods of scattering. We investigated the temperature dependence and the doping dependence both as it pertained to the inelastic scattering and to the dynamic susceptibility.

However, as the incident neutron energy was low, we were unable to explore the energy dependence of the spin dynamics over a large dynamic range. It is important to also explore this phenomenon over a long range in energy and see how it pertains to all of the features considered thus far. Theoretically, the objective is to determine both the ground state and all of the lowest lying excitations. We know that the ground state is described by the static magnetic scattering of the system. Therefore, we cannot end our investigation without probing higher energy transfers. In this vein, we will repeat all of our previous

measurements at higher energies to investigate the evolution of other low lying excitations to develop an experimental survey of this system.

The majority of these studies will be part of the focus of an upcoming PhD. However, preliminary investigations have been performed. All of the experiments to be discussed were performed on the x = 0.035 crystal considered earlier.

What we will examine here is the low temperature energy dependence of the dynamic magnetic correlations out to 30 meV. We will perform this study by considering two data sets. The first data set is a triple axis measurement that will survey phenomena from 2 meV out to 12 meV. The second data set is a preliminary analysis of a time of flight experiment that explores 5 meV to 30 meV. The conclusion of these studies is that we have quantitative agreement between the physics of this LBCO system and the physics of its sister system LSCO [4].

8.2 Lower Energy Dynamics

In the literature [4], we expect that if LBCO is the same as LSCO, then at base temperature the dispersion should reach a minimum of 8 ± 1 meV about the $(\frac{1}{2}, \frac{1}{2})$ in an x = 0.035 crystal. We are justified in this reasoning as the hour glass dispersion phenomenon is prevalent in many cuprate superconductors.

To measure this, we took an x = 0.035 LBCO crystal to the HB3 spectrometer. This spectrometer is at HFIR in Oak Ridge National Laboratories. For this experiment, we performed our experiment using orthorhombic notation

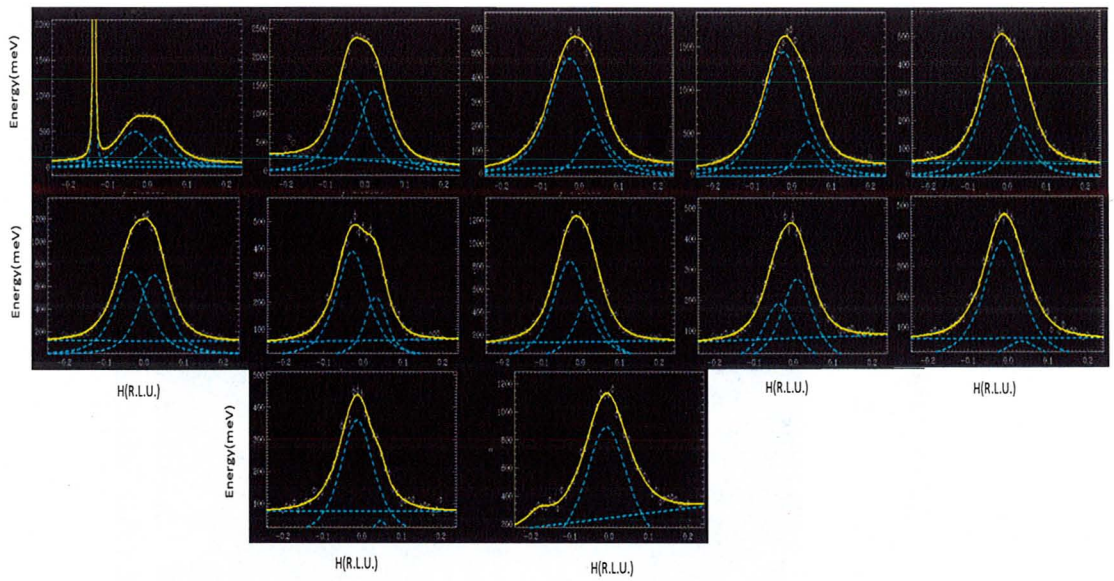

Figure 8.1: Sample raw data taken at the (010) position for various energy transfers. An attempt at fitting the data to two Lorentzian squared functions was made as well. Though this fits the data (yellow curve), the fits themselves do not seem to be as we expect for every data set. This highlights the difficulty in analyzing this data. The energy transfers in each plot are as follows. From left to right: top row: 1.7, 2.5, 3.2, 4 and 5 meV. Middle row: 6, 7, 8, 9 and 10 meV. Bottom row: 12 and 14 meV.

and aligned in the (HK0) plane. The collimation was 48-40-40-120. Measurements were performed at 1.5K. The final neutron energy for all experiments was set at 14.7 meV. We normalized our counting times to the number of neutrons that were measured by the net flux monitor. This monitor was set up between our experiment and the reactor.

Raw data is shown in figure 8.2. Notice, at the (010) position, which we note is the $(\frac{1}{2}, \frac{1}{2}, 0)$ position in tetragonal notation, we do not see a clearly two peaked structure. However, by referring to figure 8.2 we can see that what we

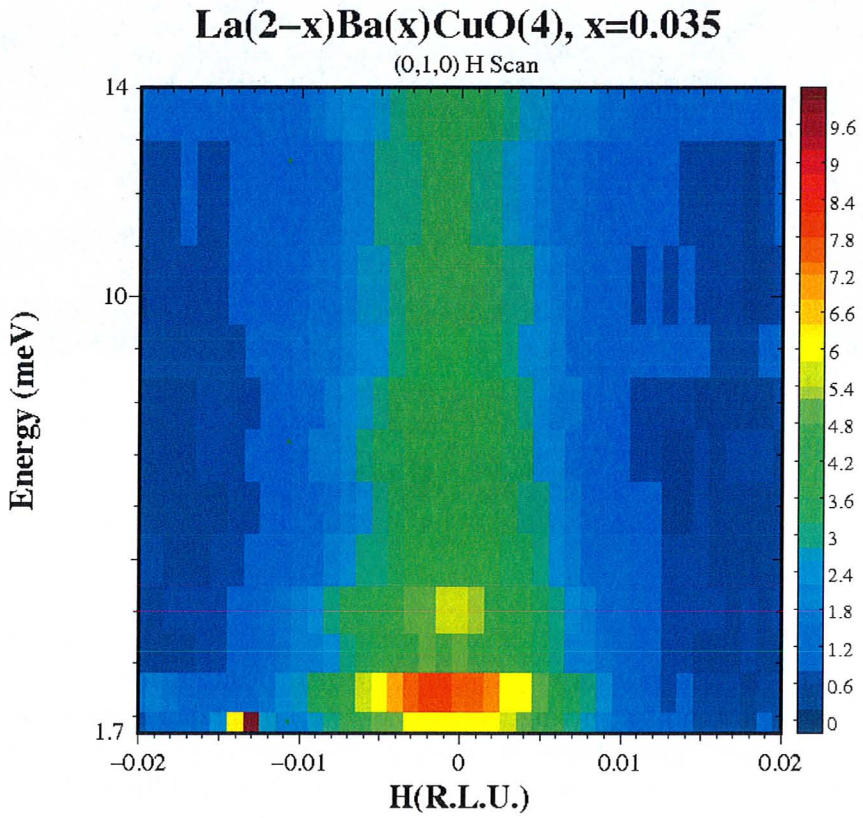

Figure 8.2: Contour plot showing all (010) line scans for various energy transfers

do have is an hour glass shaped dispersion. Furthermore, we have reason to believe we have a two peaked structure.

Thus, we have the same qualitative grounds presented in our DCS data to support our two peak hypothesis here. However, what we want is quantitative confirmation. Let us first consider the implications of an hour glass shaped energy dependence. What we first expect is that if the one signal seen is in fact comprised of two features, whose separation is varying, then it should have a width that is correspondingly varying. Additionally, if the dispersion is

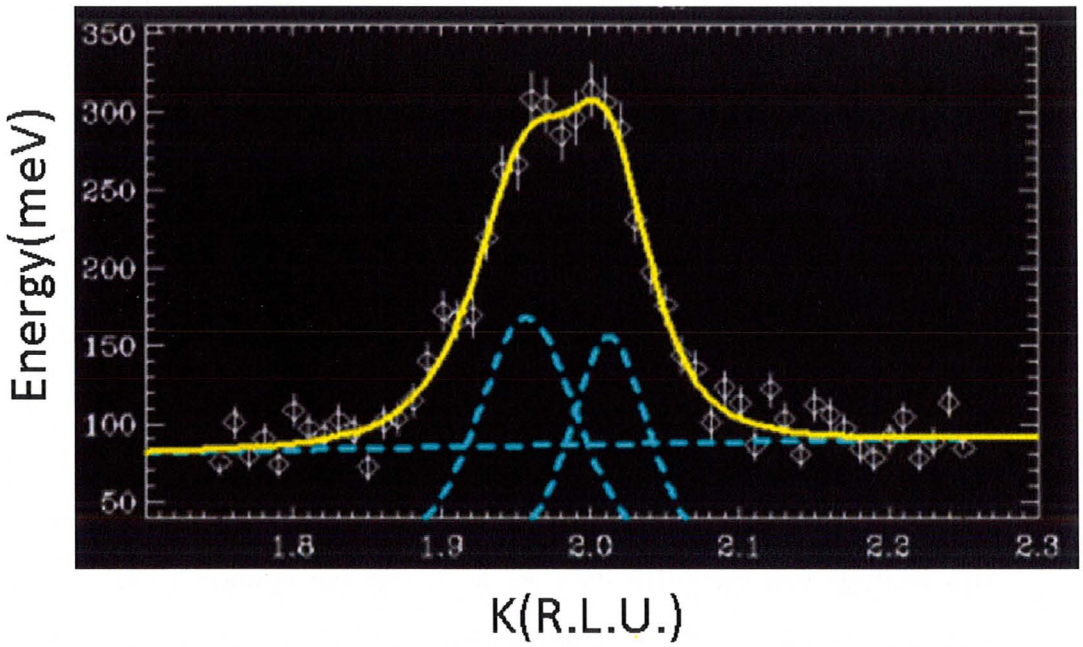

Figure 8.3: Sample data taken at the (120) position for a 10 meV energy transfer. The data has a distinct two peak structure to it, confirming the two peaked structure hypothesis.

an hour glass shape, then the composite peak should narrow and then widen. This is what we saw in the raw data.

The analysis technique that this suggests is the following. Suppose we posit effective signal positions are at these half maxima. We can then examine how the effective splitting of these signals varies as a function of energy. By carrying out the analysis in this way, we are not making any assumptions about the physics of the constituent signals themselves, i.e. their Q dependence. We can then say that this analysis is line shape independent. This gives us an accurate and precise way to analyze our data.

Before we present the results, let us note how the fits were performed. As the signal is believed to be the composite of two signals, we assumed the central limit theorem would accurately encompass our results. Hence the fit was performed with a Gaussian fit function. The analysis software used here was the PAN package in the NIST program DAVE. The best data set for this analysis was the (010) data set as it was the cleanest signal over the range of scans made. The fit function made in this way was then numerically simulated in excel with a step size along the H direction of 0.0001. From here, the maximum intensity value position was found. From this, the half maximum could be computed and hence the half maximum positions could be found numerically.

The net result of this analysis is figure 8.2. The data has been presented in a way that is reminiscent of how similar observations are presented in the literature. Comparing our result to the literature [4], we see that within error, we have quantitative agreement of the incommensuration as a function of

Figure 8.4: Numeric and line shape independent determined energy dependence of the incommensuration of the (010) peak. The method for obtaining this kind of fit is described in the text. All data points have been shifted so as to be centralized about the (010) position. The widths obtained by this analysis was then cut in half so that data points shown on either end of the (010) position could be made. This was done for ease in reconciling this data with the data seen in LSCO. For quantitative comparision, we can consider these positions to be effective peak positions. These effective peak positions are quantitativley comparable to data taken of real peak positions in x = 0.04 LSCO [4].

energy in these two systems. Please note however that we cannot say for certain that our results for the incommensurations are necessarily accurate. Regardless, they are quantitatively the same as those in LSCO. Given that it seems likely at this point that the physics of the magnetism in LBCO is the same as that in LSCO in this doping regime, this suggests that whatever the accurate incommensuration values would be, they are not dissimilar from what we have determined here.

The main interest to us here is where we find the highest density of states. The energy we determine for this phenomenon will be accurate as we expect it to be line shape independent. We determine a value of 9 ± 1 meV from this analysis. This value is also in agreement for the value determined for LSCO.

The increasingly high level of correlation between the results of LSCO and LBCO strongly suggest that the physics of the magnetism in these two systems is the same in the doping regime we have considered in this thesis. This is as we suspected would be in the case based on the hypothesis that the magnetism in this system is driven by the introduction of holes.

8.3 Higher Energy Dynamics

This research was carried out at the SEQUOIA instrument at the SNS at Oak Ridge National Laboratories. An incident neutron energy of 60 meV was selected for this experiment. This was done by using Fermi chopper 1 running at 180 Hz. All neutron fluxes were normalized on the proton charge that struck the mercury target in the SNS target building. Though measurements on four temperatures were performed, we will only the 6K data set. The crystal was

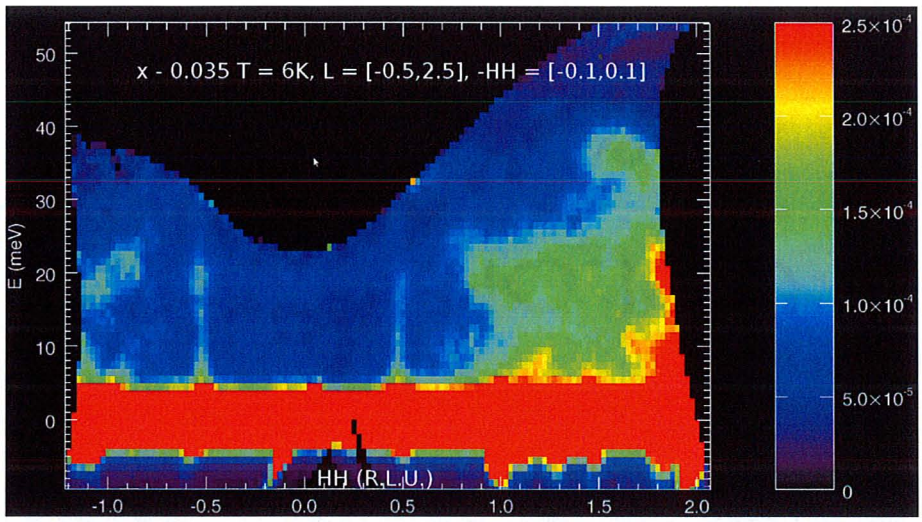

Figure 8.5: Raw data of E vs. K in x = 0.035 LBCO at 6K. The data has implicit integration of minus 0.6 to minus 0.4 in H and all L are integrated over. This data clearly shows the existence of a robust signal down to order Kelvin temperatures

mounted in a ^4He closed cycle refrigerator. The experiment was carried out in the (HHL) plane using tetragonal notation.

The first point we will make here addresses a concern raised in the DCS data set. Recall that it was claimed that the magnetism was strongest at low temperatures. Therefore there should habe been a signal at 1.5K. However, in that experiment no signal could be seen. However, as shown in figure 8.3, there is a robust signal at 6K in this data.

Now, with the lowest energies in this data set, we still must use our line shape independent method for a full and proper analysis. However, at the highest energies, we can actually resolve distinct peaks, as shown in figure 8.3. This gives us further reason to believe our hypothesis of a two peaked structure.

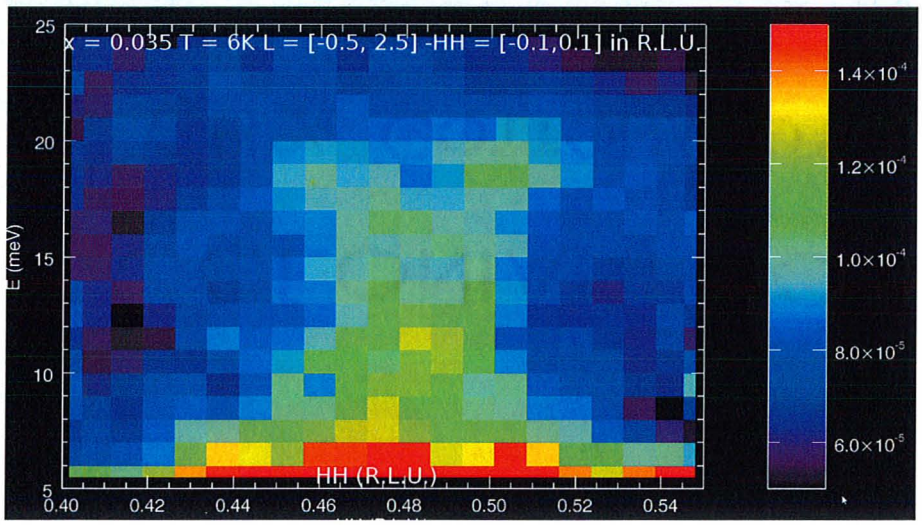

Figure 8.6: E vs HH in x = 0.035 at 6K. The data has implicit integration of minus 0.1 to 0.1 in the minus HH direction. This data set shows distinct splitting at higher energies and is suggestive of a two peaked structure

Let us try a naive line shape dependent analysis. Assume we have two Lorentzian shaped features. The idea here is we have not removed extraneous signals, such as phonons, from this data set due to a background data set not being currently available. Therefore, at this stage, our data does not merit a rigorous analysis. Nevertheless, what we will end up with after this crude analysis is a rough estimate of our peak separations. The results are shown in figure 8.3.

When this rough method of analysis is compared quantitatively to the literature [4], we find excellent agreement. This is consistent with the notion that our data is robust and that a more accurate analysis, though still necessary, will yield a picture that is similar to the one being displayed here, both qualitatively and quantitatively.

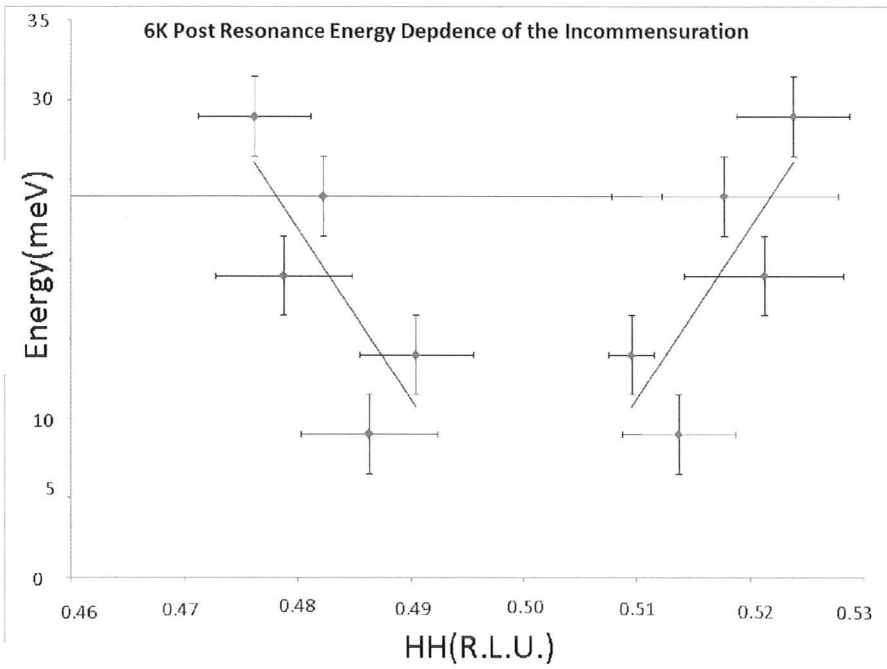

Figure 8.7: This data was obtained by assuming Lorentzian line shapes to fit of cuts through E vs. HH data set of figure 8.3, as described in the text. Note, all this data is taken past the section of the dispersion of minimum incommensuration. We therefore assume that the data can be fit with a linearly increasing function. For now, lines are added only as guides to the eye as these results are not as accurate as will be possible at a later date.

8.4 Conclusions

What we have done here is performed a survey of the dispersion of the magnetism in LBCO. This work is in its infancy. More work will be performed in the future. The reason the analysis here is rudimentary is due to hardware problems at the SNS that has only recently been resolved. The data from the SEQUOIA experiment is only now available. The first endeavour of an upcoming PhD will be to explore this data set thoroughly.

That said, the results of this survey are robust. We have developed a picture that is consistent with that of LBCO and LSCO sharing the same magnetic signals. This supports the hypothesis that these magnetic correlations have the same origin. We have further commenced an initial mapping of the dispersion of the magnetism in this system. Our analysis strongly suggests that LBCO and LSCO are in quantitative agreement. An important aspect of this agreement is that the resonance in this system is $9 \pm 1meV$. As well, by 30 meV, the incommensuration is, within error of a rough initial analysis, in agreement with the incommensuration of LSCO for a comparable doping [4]. Furthermore, we have confirmed that there are signals at the lowest temperatures, as was claimed in the previous chapter.

Chapter 9

Conclusions

What we have described here is the tail end of what has thus far been 10 years of research in Dr. Bruce Gaulin's research group. The phase diagram in chapter 7 illustratively displays the main points of this work. What should now be clear is that the subtleties of this picture are in fact contained in the spin dynamics. Going forward, it seems it will be understanding the origins of these dynamic rods that will be most important, as this phase is robust and pervades the entire phase diagram.

We have seen the doping dependence of these rods. The incommensuration clearly increases with doping and is likely 0 when x = 0. This can be seen by the increasing broadness of the scattering features and corresponding apparent reduction in rod intensity, which is really just two features separating out in Q space.

We have seen much of the temperature dependence in this system. The incommensuration is sensitive to the temperature of the sample, reducing as a function of temperature. It would be interesting to see this depenendence in full and this will be a focus in my upcoming PhD work. There is data on this

area to be analyzed and more will be collected soon. What is clear is that the rods persist out to relatively high temperatures and seem to disappear by the pseudogap temperature T*.

Lastly, we have explored the energy dependence of the rods. We have found the dispersion effect is present in this system and has an energy that is in quantitative agreement with that of LSCO. We have seen that the hour glass shape of the dispersion is maintained in this system. We also know that the rods are energy independent. That is, they persist with similar intensity all the way out to high energies. The doping dependence seems to be consistent at all energies as well. It will be interesting to see how this energy dependence is affected by temperature, as we know there is a temperature dependence to the incommensurability in this system.

Though we understand each of these phenomenon in turn, we do not yet fully grasp the overall picture that unites them all. That said, we can say with confidence that there is something that ties all these studies together. Perhaps this spine binds together magnetism, the pseudogap and superconductivity in some as of yet unimagined way. Or perhaps the connection already exists. It is unclear at this point exactly what the final result will be. But what we have seen here is that we have identified what many of the key elements in this picture will be.

Bibliography

[1] J. Tranquada. Neutron scattering studies of antiferromagnetic correlations in cuprates. *Handbook of High-Temperature Superconductivity*, 2007.

[2] T. Adachi, T. Noji, and Y. Koike. Crystal growth, transport properties, and crystal structure of the single-crystal $la_{2-x}ba_xcuo_4(x = 0.11)$. *Phys. Rev. B*, 64(14):144524, Sep 2001.

[3] B. Keimer, N. Belk, R. J. Birgeneau, A. Cassanho, C. Y. Chen, M. Greven, M. A. Kastner, A. Aharony, Y. Endoh, R. W. Erwin, and G. Shirane. Magnetic excitations in pure, lightly doped, and weakly metallic la_2cuo_4. *Phys. Rev. B*, 46(21):14034–14053, Dec 1992.

[4] M. Matsuda, M. Fujita, S. Wakimoto, J. A. Fernandez-Baca, J. M. Tranquada, and K. Yamada. Magnetic Dispersion of the Diagonal Incommensurate Phase in Lightly Doped $La_{2-x}Sr_xCuO_4$. *Phys. Rev. Lett.*, 101(19):197001, Nov 2008.

[5] Mermin N. D. Ashcroft, N. W. *Solid State Physics*. 1976.

[6] B. D. Cullity. *Elements of X-Ray Diffraction Second Edition*. November 1978.

[7] G. L. Squires. *Introduction to the Theory of Thermal Neutron Scattering*. July 1978.

[8] Oak Ridge National Labs. HB3 Spectrometer. *http://neutrons.ornl.gov/instruments/HFIR/HB3/.*

[9] NIST. DCS Spectrometer. *http://neutrons.ornl.gov/instruments/HFIR/HB3/.*

[10] S. R. Dunsiger, Y. Zhao, B. D. Gaulin, Y. Qiu, P. Bourges, Y. Sidis, J. R. D. Copley, A. Kallin, E. M. Mazurek, and H. A. Dabkowska. Diagonal and collinear incommensurate spin structures in underdoped $la_{2-x}ba_xcuo_4$. *Phys. Rev. B*, 78(9):092507, Sep 2008.

[11] G. van Gastel. *Neutron Scattering Studies of* $La_{2-x}Ba_xCuO_4$. 2009.

[12] M. Fujita, H. Goka, K. Yamada, J. M. Tranquada, and L. P. Regnault. Stripe order, depinning, and fluctuations in $La_{1.875}Ba_{0.125}CuO_4$ and $La_{1.875}Ba_{0.075}Sr_{0.050}CuO_4$. *Phys. Rev. B*, 70(10):104517, Sep 2004.

[13] Possible High T_c Superconductivity in the $Ba - La - Cu - O$ System.

[14] J. Bardeen, L. N. Cooper, and J. R. Schrieffer. Theory of superconductivity. *Phys. Rev.*, 108(5):1175–1204, Dec 1957.

[15] D.L. Nicolas, P. Auban-Senzier, S. Rene de Cotret, and D. Jerome K. Bechgaard Louis Taillefer A. Sedeki, C. Bourbonnais. Correlation between linear resistivity and tc in organic and pnictide superconductors. *arXiv:0905.0964v1.*

[16] M Norman.

[17] P. Böni, J. D. Axe, G. Shirane, R. J. Birgeneau, D. R. Gabbe, H. P. Jenssen, M. A. Kastner, C. J. Peters, P. J. Picone, and T. R. Thurston.

Lattice instability and soft phonons in single-crystal $La_{2-x}Sr_xCuO_4$. *Phys. Rev. B*, 38(1):185–194, Jul 1988.

[18] S. A. Kivelson, I. P. Bindloss, E. Fradkin, V. Oganesyan, J. M. Tranquada, A. Kapitulnik, and C. Howald. How to detect fluctuating stripes in the high-temperature superconductors. *Rev. Mod. Phys.*, 75(4):1201–1241, Oct 2003.

[19] N. Bulut, D. Hone, D. J. Scalapino, and N. E. Bickers. Random-phase-approximation analysis of nmr and neutron-scattering experiments on layered cuprates. *Phys. Rev. Lett.*, 64(22):2723–2726, May 1990.

[20] Y. Zhao. *X-Ray and Neutron Scattering Studies of Underdoped $La_{2-x}Ba_xCuO_4$ Single Crystals.* 2008.

[21] D. Griffiths. *Introduction to Elementary Particles.* March 1987.

[22] G. Shirane, S. M. Shapiro, and J. M. Tranquada. *Neutron Scattering with a Triple-Axis Spectrometer.* March 2002.

[23] D. M. Ginsberg. *Physical Properties of High Temperature Superconductors I.* 1989.

[24] Y. Zhao, B. D. Gaulin, J. P. Castellan, J. P. C. Ruff, S. R. Dunsiger, G. D. Gu, and H. A. Dabkowska. High-resolution x-ray scattering studies of structural phase transitions in underdoped $la_{2-x}ba_xcuo_4$. *Phys. Rev. B*, 76(18):184121, Nov 2007.

[25] T. R. Thurston, P. M. Gehring, G. Shirane, R. J. Birgeneau, M. A. Kastner, Y. Endoh, M. Matsuda, K. Yamada, H. Kojima, and

I. Tanaka. Low-energy incommensurate spin excitations in superconducting $la_{1.85}sr_{0.15}cuo_4$. *Phys. Rev. B*, 46(14):9128–9131, Oct 1992.

[26] M. Matsuda, K. Yamada, Y. Endoh, T. R. Thurston, G. Shirane, R. J. Birgeneau, M. A. Kastner, I. Tanaka, and H. Kojima. Spin fluctuations in superconducting $la_{1.85}sr_{0.15}cuo_4$. *Phys. Rev. B*, 49(10):6958–6966, Mar 1994.

[27] Masaru Kato, Kazushige Machida, Hiizu Nakanishi, and Mitsutaka Fujita. Soliton lattice modulation of incommensurate spin density wave in two dimensional hubbard model -a mean field study-. *Journal of the Physical Society of Japan*, 59(3):1047–1058, 1990.

[28] S. Shamoto, M. Sato, J. M. Tranquada, B. J. Sternlieb, and G. Shirane. Neutron-scattering study of antiferromagnetism in $yba_2cu_3o_{6.15}$. *Phys. Rev. B*, 48(18):13817–13825, Nov 1993.

[29] M. Fujita, H. Goka, K. Yamada, J. M. Tranquada, and L. P. Regnault. Stripe order, depinning, and fluctuations in $la_{1.875}ba_{0.125}cuo_4$ and $la_{1.875}ba_{0.075}sr_{0.050}cuo_4$. *Phys. Rev. B*, 70(10):104517, Sep 2004.

[30] B. Keimer, R. J. Birgeneau, A. Cassanho, Y. Endoh, R. W. Erwin, M. A. Kastner, and G. Shirane. Scaling behavior of the generalized susceptibility in $la_{2-x}sr_xcuo_{4+y}$. *Phys. Rev. Lett.*, 67(14):1930–1933, Sep 1991.

[31] M. Matsuda, Y. S. Lee, M. Greven, M. A. Kastner, R. J. Birgeneau, K. Yamada, Y. Endoh, P. Böni, S.-H. Lee, S. Wakimoto, and G. Shirane. Freezing of anisotropic spin clusters in $la_{1.98}sr_{0.02}cuo_4$. *Phys. Rev. B*, 61(6):4326–4333, Feb 2000.

[32] S. M. Hayden, G. Aeppli, H. Mook, D. Rytz, M. F. Hundley, and Z. Fisk. Magnetic fluctuations in $la_{1.95}ba_{0.05}cuo_4$. *Phys. Rev. Lett.*, 66(6):821–824, Feb 1991.

[33] Chul-Ho Lee, Kazuyoshi Yamada, Yasuo Endoh, Gen Shirane, R. J. Birgeneau, M. A. Kastner, M. Greven, and Y-J. Kim. Energy spectrum of spin fluctuations in superconducting $la_{2-x}sr_xcuo_4$ ($0.10 \leq x \leq 0.25$). *Journal of the Physical Society of Japan*, 69(4):1170–1176, 2000.

[34] O. J. Lipscombe, S. M. Hayden, B. Vignolle, D. F. McMorrow, and T. G. Perring. Persistence of high-frequency spin fluctuations in overdoped superconducting $la_{2-x}sr_xcuo_4$ ($x = 0.22$). *Phys. Rev. Lett.*, 99(6):067002, Aug 2007.

[35] Andrei S. Mishchenko and Naoto Nagaosa. Theory of excitation spectra of electron–phonon coupled systems. *Journal of the Physical Society of Japan*, 75(1):011003, 2006.

[36] Jungho Kim, A. Kagedan, G. D. Gu, C. S. Nelson, and Young-June Kim. Magnetic field dependence of charge stripe order in $la_{2-x}ba_xcuo_4$ ($x \approx \frac{1}{8}$). *Phys. Rev. B*, 77(18):180513, May 2008.

[37] D. Reznik, L. Pintschovius, M. Ito, S. Iikubo, M. Sato, H. Goka, M. Fujita, K. Yamada, G. D. Gu, and J. M. Tranquada. Electron-phonon coupling reflecting dynamic charge inhomogeneity in copper oxide superconductors. *Nature*, 440:1170–1173, April 2006.

[38] M. Matsuda, M. Fujita, K. Yamada, R. J. Birgeneau, Y. Endoh, and G. Shirane. Electronic phase separation in lightly doped $la_{2-x}sr_xcuo_4$. *Phys. Rev. B*, 65(13):134515, Mar 2002.

[39] R. J. Birgeneau, N. Belk, Y. Endoh, R. W. Erwin, M. A. Kastner, B. Keimer, and G. Shirane. Static and dynamic spin fluctuations in the spin glass doping regime in $La_{2-x}Sr_xCuO_{4+\delta}$. *Physica B Condensed Matter*, 180:15–20, June 1992.

[40] J. M. Tranquada, H. Woo, T. G. Perring, H. Goka, G. D. Gu, G. Xu, M. Fujita, and K. Yamada. Quantum magnetic excitations from stripes in copper oxide superconductors. *Nature*, 429:534–538, June 2004.

[41] S. R. Dunsiger, Y. Zhao, Z. Yamani, W. J. L. Buyers, H. A. Dabkowska, and B. D. Gaulin. Incommensurate spin ordering and fluctuations in underdoped $la_{2x}ba_xcuo_4$. *Phys. Rev. B*, 77(22):224410–+, June 2008.

[42] N. Doiron-Leyraud, C. Proust, D. Leboeuf, J. Levallois, J.-B. Bonnemaison, R. Liang, D. A. Bonn, W. N. Hardy, and L. Taillefer. Quantum oscillations and the Fermi surface in an underdoped high-T_c superconductor. *Nature*, 447:565–568, May 2007.

[43] C. Kittel. *Introduction to Solid State Physics*. 2005.